Tracking and Data Fusion Applications

Wolfgang Koch

FGAN-FKIE
Neuenahrer Strasse 20
D 53343 Wachtberg, Germany
Tel +49 228 9435 373
Fax +49 228 9435 685

email w.koch@fgan.de

Abstract

In many engineering applications, including surveillance, guidance, or navigation, single stand-alone sensors or sensor networks are used for collecting information on time varying quantities of interest, such as kinematical characteristics and measured attributes of moving or stationary objects of interest (e.g. maneuvering air targets, ground moving vehicles, or stationary movers such as a rotating antennas).

More strictly speaking, in these applications the state vectors of stochastically moving objects are to be estimated from a series of sensor data sets, also called scans or data frames. The individual measurements are produced by the sensors at discrete instants of time, being referred to as scan or frame time, target revisit time, or data innovation time. These output data (sensor reports, observations, returns, hits, plots) typically result from complex estimation procedures themselves characterizing particular waveform parameters of the received sensor signals (signal processing).

In case of moving point-source objects or small extended objects, i.e. typical radar targets, often relatively simple statistical models can be derived from basic physical laws describing their temporal behavior and thus defining the underlying dynamical system. In addition, appropriate sensor models are available or can be constructed, which characterize the statistical properties of the produced sensor data sufficiently correct.

As an introduction to ***target tracking and data fusion applications*** *characteristic problems occurring in typical radar applications are presented; key ideas relevant for their solution are discussed.*

Koch, W. (2007) Tracking and Data Fusion Applications. In *Advanced Radar Systems, Signal and Data Processing* (pp. 9-1 – 9-36). Educational Notes RTO-EN-SET-086bis, Paper 9. Neuilly-sur-Seine, France: RTO. Available from: http://www.rto.nato.int/abstracts.asp.

Contents

1 Adaptive Tracking for Phased-array Radar

Modern phased-array radars call for tracking algorithms that efficiently exploit all degrees of freedom available, which are variable over a wide range and can be chosen individually for each track. This is particularly true for military air situations where both, agile targets and targets significantly differing in their radar cross section, must be taken into account. Unless properly handled, such situations can be highly allocation time and energy consuming. In this context adaptive techniques for combined tracking and sensor management are discussed, i.e. control of data innovation intervals, radar beam positioning, and transmitted energy. By efficient exploitation of the limited resources the total surveillance performance of the sensor system can be improved.

1.1 General Overview

In military applications often distinct maneuvering phases exist as even agile targets do not permanently maneuver. Nevertheless, abrupt transitions to high-g turns can well occur. Allocation time and energy savings are thus to be expected if adaptive target dynamics models are used[2, 4, 11, 20], such as Interacting Multiple Model (IMM). Besides their kinematical characteristics, the mean radar cross section (RCS) of the targets is usually unknown and variable over a wide range. By processing of signal amplitude information, however, the energy spent for track maintenance can be adapted to the actual target strength. Also by this measure the total sensor load can significantly be reduced.

Due to the locally confined target illumination by the pencil-beam of a phased-array, abrupt transitions into maneuvering flight phases are critical as, in contrast to conventional radar, a periodic target illumination is no longer guaranteed. Any track reiinitiation is thus highly allocation time and energy consuming and in addition locks the sensor for other tasks (e.g. weapon guidance). This calls for intelligent algorithms for beam positioning and local search [8] that are crucial for phased-array tracking.

For radars scanning the field of view at a constant rate (TWS: Track-while-scan), the BAYESian tracking techniques, discussed in the first talk provide an iterative updating scheme for conditional probability densities of the target state given all sensor data and a priori information available. In those applications data acquisition and tracking are completely decoupled. For phased-array radar, however, the current signal-to-noise ratio of the target (i.e. the detection probability) strongly depends on the correct positioning of the pencil-beam which is now taken into the responsibility of the tracking system. Thus sensor control and data processing are closely interrelated. This basically *local* character of the tracking process constitutes the principal difference between phased-array and TWS applications from a tracking point of view. By using a suitable sensor model, however, this fact can be incorporated into the BAYESian formalism.

Figure 1 provides a simplified schematic overview of phased-array radar function control with the corresponding flow of information.

1.2 Modeling Assumptions

Resource management for a multi-functional phased-array radar certainly depends on the particular application considered. We here discuss track maintenance for ground-based air surveillance while minimizing the allocation time and energy required. The track accuracy is important only in so far as stable tracks are guaranteed. Track initiation or implementation issues are not addressed here. To make the benefits of IMM modeling and amplitude information clearly visible, false detections (clutter, ECM), data association conflicts, or possibly unresolved measurements were excluded from the discussion. Nevertheless, their impact might well be incorporated into the general BAYESian framework sketched in the first talk (see also [7]).

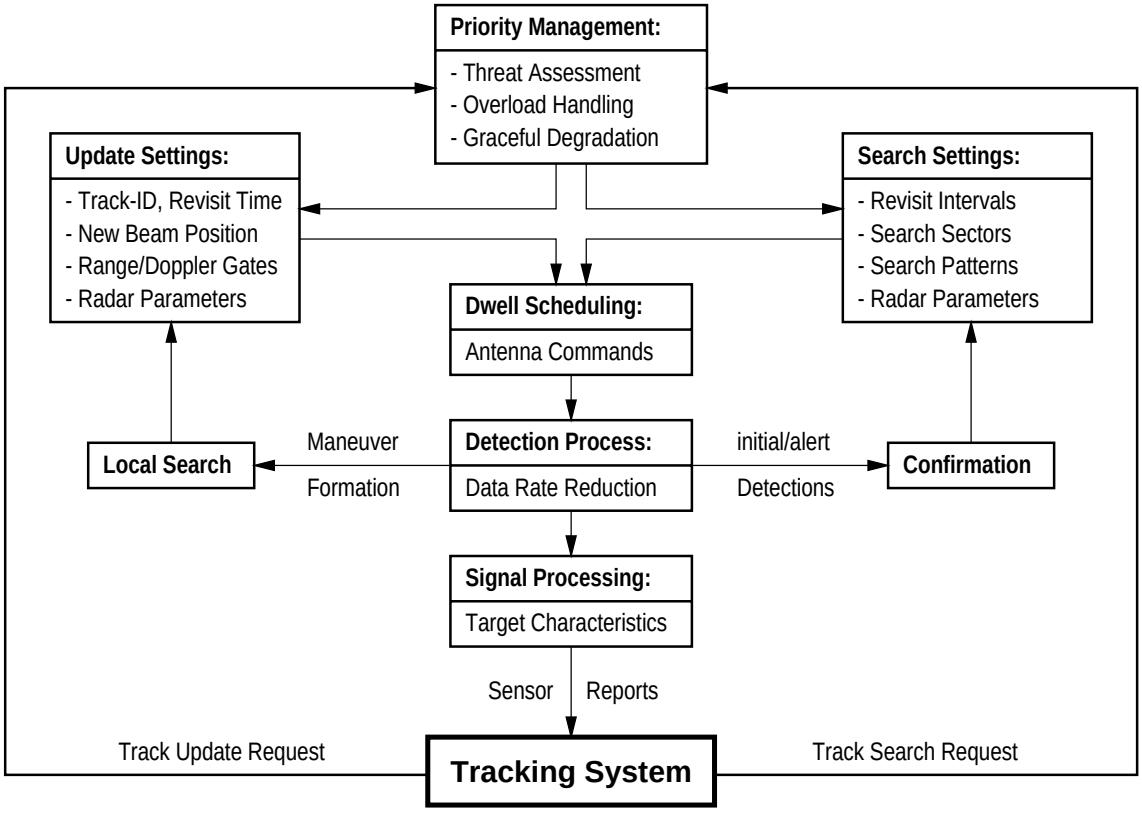

Figure 1: Phased-Array Radar Function Control (Flow of Information)

1.2.1 Resource Allocation

In phased-array tracking additional sensor information can be acquired when needed. Before each 'radar resource allocation' [4] certain radar parameters must be selected by the tracking system depending on the current lack of information. We here consider the *target revisit time* t_k, the current *beam position* $\mathbf{b}_k$ and the transmitted *energy per dwell* e_k. Other parameters, such as detection threshold λ_D or beam width B, are assumed to be constant. After processing the skin echo, the resource allocation R_k at time t_k results in measurements of direction cosines and target range, $\mathbf{z}_k = (\bar{u}_k, \bar{v}_k, \bar{r}_k)$, along with the signal amplitude a_k. Possibly a single dwell is not sufficient for target detection and a subsequent fine localization. Let n_{b_k} denote the number of dwells for a successful detection along with the corresponding beam positions $B_k = \{\mathbf{b}_k^i\}_{i=1}^{n_{b_k}}$. Each allocation is thus characterized by the tuple $R_k = (t_k, B_k, n_{b_k}, e_k, \mathbf{z}_k, a_k)$. The sequence of successive allocations is denoted by $\mathcal{Z}^k = \{R_k, \mathcal{Z}^{k-1}\}$.

1.2.2 RCS Fluctuations

The instantaneous radar cross section σ_k of realistic targets strongly depends on the radar frequency used and the current aspect angle. For this reason, statistical models are used for describing the backscattering properties of the targets. In many practical cases σ_k is described by gamma-densities:

$$p(\sigma_k|\bar{\sigma}, m) = \mathcal{G}_m\left(\sigma_k; \bar{\sigma}\right) \tag{1}$$

$$= \frac{(m/\bar{\sigma})^m}{\Gamma(m)}\, \sigma_k^{m-1}\, \mathrm{e}^{-\sigma_k(m/\bar{\sigma})}. \tag{2}$$

In this equation $\bar{\sigma}$ denotes the mean RCS of the target that is usually unknown, but constant in time and characteristic of a certain class of targets. The individual samples σ_k are assumed to be statistically independent

for subsequent dwells (guaranteed by frequency decorrelation, e.g.). The cases $m = 1, 2$ are referred to as Swerling-I and -III fluctuations[3].

Let the instantaneous target signal $\mathbf{v}_k = (v_1, v_2)$ be additively corrupted by GAUSSian noise with variance σ_n^2. As the signal components are assumed to be statistically independent, the pdf of the resultant signal $\mathbf{s}_k = (s_1, s_2)$ is therefore given by a product of GAUSSians:

$$p(\mathbf{s}_k|\mathbf{v}_k) = \mathcal{N}\left(s_1;\, v_1,\, \sigma_n^2\right)\, \mathcal{N}\left(s_2;\, v_2,\, \sigma_n^2\right). \tag{3}$$

The normalized scalar quantity $a_k^2 = (s_1^2+s_2^2)/2\sigma_n^2$ derived from the vector signal $\mathbf{s}_k$ is RICEian distributed[3]:

$$p(a_k^2|\mathrm{sn}_k) = \mathrm{e}^{-a_k^2-\mathrm{sn}_k}\, I_0\left(2a_k\sqrt{\mathrm{sn}_k}\right) \qquad \text{with:} \quad \mathrm{sn}_k = (v_1^2 + v_2^2)/2\sigma_n^2. \tag{4}$$

Hence, sn_k denotes the instantaneous signal-to-noise ratio of the target being proportional to σ_k. Its expectation with of respect to $p(a_k^2|\mathrm{sn}_k)$ is $\mathbb{E}[a_k^2] = 1 + \mathrm{sn}_k$; pure noise ($\mathrm{sn}_k = 0$) has thus unit power. Due to the RCS model previously discussed, sn_k is gamma-distributed with the mean SN: $p(\mathrm{sn}_k|\mathrm{SN}) = \mathcal{G}_m\left(\mathrm{sn}_k;\, \mathrm{SN}\right)$. The conditional density of a_k^2 given SN is thus obtained by [1]:

$$p(a_k^2|\mathrm{SN}) = \int_0^\infty d\mathrm{sn}_k\; p(a_k^2|\mathrm{sn}_k)\; p(\mathrm{sn}_k|\mathrm{SN}) \tag{5}$$

$$= \left(\tfrac{m+\mathrm{SN}}{m}\right)^{-m} \mathrm{e}^{-ma_k^2/(m+\mathrm{SN})}\; L_{m-1}\left(\tfrac{-a_k^2\mathrm{SN}}{m+\mathrm{SN}}\right), \tag{6}$$

where L_{m-1} denotes the Laguerre polynomials. For Swerling-I/III: $L_0(-x) = 1$, $L_1(-x) = 1 + x$. Evidently, $p(a_k^2|\mathrm{SN})$ can be interpreted as a gamma mixture with $\mathbb{E}[a_k^2] = 1 + \mathrm{SN}$.

1.2.3 Signal-to-Noise Ratio

Any sensor model for phased-array tracking has to provide a functional relationship between the expected signal-to-noise ratio SN_k at time t_k, the sensor parameters (transmitted energy, beam position) and the target parameters (mean RCS, target position). With a GAUSSian beam form[8] and using the radar range equation we assume:

$$\mathrm{SN}_k = \mathrm{SN}_0 \left(\tfrac{\bar{\sigma}}{\bar{\sigma}_0}\right) \left(\tfrac{e_k}{e_0}\right) \left(\tfrac{r_k}{r_0}\right)^{-4} \mathrm{e}^{-2\Delta b_k} \tag{7}$$

$$\text{with} \quad \Delta\mathbf{b}_k = (u_k - b_k^u)^2/B_k + (v_k - b_k^v)^2/B^2. \tag{8}$$

r_k is the actual target range at time t_k while u_k, v_k denote the related direction cosines. With the beam position $\mathbf{b}_k = (b_k^u, b_k^v)$ and the (one-sided) beam width B, $\Delta\mathbf{b}_k$ is a measure of relative beam positioning error. The radar parameter SN_0 is the expected mean signal-to-noise ratio of a target with a standard mean cross section $\bar{\sigma}_0$ at a reference range r_0 that is directly ($\Delta\mathbf{b}_k = \mathbf{o}$) illuminated by the beam with the energy e_0. Due to the functional relationship stated in Equation 6 the signal strength a_k^2 can be interpreted as a measurement of $\bar{\sigma}$.

1.2.4 Detection/Measurements

A detection is assumed if the received signal strength exceeds a certain detection threshold: $a_k^2 > \lambda_D$. For a given m in the fluctuation model (Equation 2), the detection probability P_D is a function of SN and λ_D:

$$P_D(\mathrm{SN}, \lambda_D, m) = \int_{\lambda_D}^\infty da_k^2\; p(a_k^2|\mathrm{SN}). \tag{9}$$

The false alarm probability P_F is analogously obtained:

$$P_F(\lambda_D) = P_D(0, \lambda_D, m) = \mathrm{e}^{-\lambda_D}. \tag{10}$$

Integration results in explicit expressions for P_D[3]. For Swerling-I/III fluctuations we obtain:

$$P_D^I(\mathrm{SN}, \lambda_D) = \mathrm{e}^{-\frac{\lambda_D}{1+\mathrm{SN}}} = P_F^{\frac{1}{1+\mathrm{SN}}} \tag{11}$$

$$P_D^{III}(\mathrm{SN}, \lambda_D) = \mathrm{e}^{-\frac{\lambda_D}{1+\mathrm{SN}/2}} \left(1 + \frac{(\mathrm{SN}/2)\lambda_D}{(1+\mathrm{SN}/2)^2}\right). \tag{12}$$

For target tracking a_k^2 is available after a detection, i.e. $a_k^2 > \lambda_D$. We thus need the conditional density:

$$p(a_k^2 | a_k^2 > \lambda_D, \mathrm{SN}, m) = \begin{cases} p(a_k^2|\mathrm{SN}) / P_D(\mathrm{SN}, \lambda_D, m) & \text{for} \quad a_k^2 > \lambda_D \\ 0 & \text{for} \quad a_k^2 \leq \lambda_D \end{cases}. \tag{13}$$

For strong targets we can assume $\mathrm{SN} \approx 1 + \mathrm{SN} \approx \ldots \approx m + \mathrm{SN}$ and thus approximately obtain:

$$p(a_k^2|\mathrm{SN}) \approx \left(\tfrac{\mathrm{SN}}{m}\right)^{-m} \mathrm{e}^{-m a_k^2/\mathrm{SN}} \, L_{m-1}\left(-a_k^2\right) \tag{14}$$

(see Equation 6). On the other hand, let the detection probability for $m \neq 1$ be approximately given by: $P_D(\mathrm{SN}, \lambda_D, m) \approx P_D^I(\mathrm{SN}, \lambda_D)$ (i.e. Swerling I). We can therefore write:

$$p(a | a_k^2 > \lambda_D, \mathrm{SN}, m) \approx \mathcal{S}_m\left(a_k^2; \mathrm{SN}\right) \tag{15}$$

$$\text{with} \quad \mathcal{S}_m\left(a_k^2; \mathrm{SN}\right) = \begin{cases} \left(\tfrac{\mathrm{SN}}{m}\right)^{-m} \mathrm{e}^{-(m a_k^2 + \lambda_D)/\mathrm{SN}} \, L_{m-1}\left(-a_k^2\right) & \text{for} \quad a_k^2 > \lambda_D \\ 0 & \text{for} \quad a_k^2 \leq \lambda_D. \end{cases} \tag{16}$$

Let us assume that monopulse localization after detection result in bias-free measurements u_k', v_k' of the direction cosines and range with GAUSSian measurement errors. According to [3] the standard deviations $\sigma_k^{u,v}$ depend on the beam width B and the instantaneous sn_k in the following manner: $\sigma_k^{u,v} \propto B/\sqrt{\mathrm{sn}_k} \approx B/\sqrt{a_k^2 - 1}$. As sn_k is unknown, in the last approximation a_k^2 is used as a bias-free estimate of sn_k ($\mathbb{E}[a_k^2] = 1 + \mathrm{sn}_k$). The range error is assumed to be GAUSSian with a constant standard deviation σ^r. Evidently, this model of the measurement process does not depend on the RCS fluctuation model.

1.2.5 IMM Dynamics Model

Systems with MARKOVian switching coefficients [2] are well-suited for modeling the different phases in a mission. They are represented by multiple dynamics models with a given probability of switching between the models. Let i_k denote the dynamics model indexed by i_k at time t_k. The transition probabilities are thus part of the modeling assumptions, however a priori unknown in a real application. Fortunately, the tracking performance does not seem to depend critically on their particular choice [4]. The related MARKOV process is described by:

$$p(\mathbf{x}_k, i_k | \mathbf{x}_{k-1}, i_{k-1}) = p_{i_k i_{k-1}} \; \mathcal{N}(\mathbf{x}_k; \mathbf{F}_{i_k}\mathbf{x}_{k-1}, \mathbf{Q}_{i_k}), \quad 1 \leq i_k, i_{k-1} \leq r. \tag{17}$$

Hence, the model jump process is a MARKOV chain with model transition probabilities $p_{i_k i_{k-1}} = p(i_k|i_{k-1})$, the individual models being linear-GAUSSian. $\mathbf{F}_{i_k}$ denotes the evolution matrix, while $\mathbf{D}_{i_k}$ reflects the maneuvering capability of the model indexed by i_k.

1.3 Adaptive Track Maintenance

As discussed in the previous talk, tracking is an iterative updating scheme for conditional probability densities $p(\mathbf{x}_k|\mathcal{Z}^k)$ that describe the current target state $\mathbf{x}_k$ given all available resource allocations $\mathcal{Z}^k$ and the underlying a priori information in terms of statistical models. Essentially, the update consists of a prediction step followed by filtering. The knowledge of the target state at time t_k before a new allocation has taken place is given by $p(\mathbf{x}_{k+1}|\mathcal{Z}^k)$. Allocation decisions for a certain time must thus be based on this density that essentially depends on the underlying dynamics model.

1.3.1 BAYESian IMM-MHT

Due to the Total Probability Theorem, dynamics modeling according to IMM results in finite mixture densities:

$$p(\mathbf{x}_k|\mathcal{Z}^k) = \sum_{\mathbf{i}_k} p(x_k|\mathbf{i}_k, \mathcal{Z}^k)\, p(\mathbf{i}_k|\mathcal{Z}^k) \tag{18}$$

with $\mathbf{i}_k = \{i_k, \ldots, i_1\}$ denoting a particular *model history*, i.e. a sequence of possible hypotheses regarding the target dynamics model from the initial observation up to the most recent measurement at time t_k. This is in analogy to the discussion in the previous talk. As the number of terms in Equation 18 exponentially increases with increasing k, various techniques have been developed for approximately representing $p(\mathbf{x}_k|\mathcal{Z}^k)$ by mixtures with a *constant* number of components at each t_k. With $\mathbf{i}_n^k = \{i_k, \ldots, i_{k-n+1}\}$ denoting a sequence of possible model hypotheses "n scans back", we are looking for approximations by *Normal Mixtures*,

$$p(\mathbf{x}_k|\mathcal{Z}^k) \approx \sum_{\mathbf{i}_n^k} \boldsymbol{\mu}_{\mathbf{i}_n^k}\ \mathcal{N}(\mathbf{x}_k;\, \mathbf{x}_{\mathbf{i}_n^k},\, \mathbf{P}_{\mathbf{i}_n^k}), \tag{19}$$

with $\boldsymbol{\mu}_{\mathbf{i}_n^k} = p(\mathbf{i}_n^k|\mathcal{Z}^k)$ and $\mathcal{N}(\mathbf{x}_k;\, \mathbf{x}_{\mathbf{i}_n^k},\, \mathbf{P}_{\mathbf{i}_n^k}) = p(\mathbf{x}_k|\mathbf{i}_n^k, \mathcal{Z}^k)$. Due to BAYES' Rule, $\mathbf{x}_{\mathbf{i}_n^k}$ and $\mathbf{P}_{\mathbf{i}_n^k}$ of each mixture component are iteratively obtained by formulae essentially based on KALMAN filtering. Also the weighting factors $\boldsymbol{\mu}_{\mathbf{i}_n^k}$ obey simple formulae[2, 16]. In case of a single dynamics model ($r = 1$), the conditional densities $p(\mathbf{x}_k|\mathcal{Z}^k)$ are strictly given by GAUSSians; i.e. the filtering loop is simply KALMAN filtering.

For $n = 1$, $p(\mathbf{x}_k|\mathcal{Z}^k)$ is approximated by a mixture with r components according to the r dynamics models used. GPB2 and standard IMM algorithms are possible realizations of this scheme [2]. For standard IMM the approximations are made after the prediction, but before the filtering step, while for GPB2 they are applied after the filtering step. Hence, GPB2 requires some more computational effort. More generally speaking, the basic idea of standard IMM (moment matching directly after the prediction step) may easily be adopted to $n > 2$ providing a more accurate approximation of the densities $p(\mathbf{x}_k|\mathcal{Z}^k)$ than for $n = 2$. At each stage k of the tracking loop the parameters $\boldsymbol{\mu}_{\mathbf{i}_n^k}$, $\mathbf{x}_{\mathbf{i}_n^k}$, $\mathbf{P}_{\mathbf{i}_n^k}$ approximately represent the density $p(\mathbf{x}_k|\mathcal{Z}^k)$.

1.3.2 RCS as a State Variable

Let us treat the normalized mean RCS of the target, $s_k = \bar{\sigma}_k/\bar{\sigma}_0$, as an additional component of the state vector. As the signal strength after detection may be viewed as a measurement of s_k, let us consider the conditional density $p(\mathbf{x}_k, s_k|\mathcal{Z}^k) = p(s_k|\mathbf{x}_k, \mathcal{Z}^k)\, p(\mathbf{x}_k|\mathcal{Z}^k)$. The calculation of $p(\mathbf{x}_k|\mathcal{Z}^k)$ was discussed above. For $p(s_k|\mathbf{x}_k, \mathcal{Z}^k)$ BAYES' Rule yields up to a normalizing constant:

$$p(s_k|\mathbf{x}_k, a_k^2, \mathcal{Z}^{k-1}) \propto \mathcal{S}_m\big(a_k^2;\, \mathrm{SN}\big)\ p(s_k|\mathbf{x}_k, \mathcal{Z}^{k-1}). \tag{20}$$

Let us assume that $p(s_k|\mathbf{x}_k, \mathcal{Z}^{k-1})$ are given by inverse gamma densities:

$$p(s_k|\mathbf{x}_k, \mathcal{Z}^{k-1}) = \mathcal{I}_{\mu_{k|k-1}}\big(s_k;\, \hat{s}_{k|k-1}\big) \tag{21}$$

$$\text{with:}\quad \mathcal{I}_{\mu}\big(s;\, \hat{s}\big) = \big[((\mu-1)\hat{s})^{\mu}/\Gamma(\mu)\big]\ s^{-\mu-1}\ \mathrm{e}^{-\frac{(\mu-1)\hat{s}}{s}} \tag{22}$$

defined by $\hat{s} = \mathbb{E}[s] > 0$ and a parameter $\mu > 1$. For $\mu > 2$ the related variance exists: $\mathbb{V}[s] = \hat{s}^2/(\mu-2)$. This class of densities is invariant under the successive application of BAYES Rule according to Equation 20, for up to normalization we obtain:

$$\mathcal{S}_m\big(a_k^2;\, \mathrm{SN}\big)\ \mathcal{I}_{\mu_{k|k-1}}\big(s_k;\, \hat{s}_{k|k-1}\big) \propto$$

$$\alpha_k^{-m}\ s_k^{-\mu_{k|k-1}-m-1}\ \exp\Big(-\frac{(\mu_{k|k-1}-1)\hat{s}_{k|k-1}+\frac{ma_k^2+\lambda_D}{\alpha_k}}{s_k}\Big) \propto \mathcal{I}_{\mu_k}\big(s_k;\, \hat{s}_k\big) \tag{23}$$

$$\text{with:} \qquad \alpha_k = \mathrm{SN}_0 \left(\frac{e_k}{e_0}\right) \left(\frac{r_k}{r_0}\right)^{-4} \mathrm{e}^{-2\Delta b_k} \tag{24}$$

$$\hat{s}_k = \frac{\mu_{k|k-1}-1}{\mu_{k|k-1}+m-1} \hat{s}_{k|k-1} + \frac{(m a_k^2 + \lambda_D)/\alpha_k}{\mu_{k|k-1}+m-1} \tag{25}$$

$$\mu_k = \mu_{k|k-1} + m. \tag{26}$$

With reference to s_k the density $\mathcal{I}_{\mu_k}\left(s_k;\, \hat{s}_k\right)$ is correctly normalized. Due to $\alpha_k = \alpha_k(r_k, u_k, v_k)$, however, it depends on the target position. In order to preserve the factorization of $p(\mathbf{x}_k, s_k|\mathcal{Z}^k)$ in a normal mixture related to $\mathbf{x}_k$ and an inverse gamma density related to s_k we use the approximation:

$$\alpha_k \approx \left(\frac{e_k}{e_0}\right) \left(\frac{\hat{\mathbf{r}}_k}{r_0}\right)^{-4} \mathrm{e}^{-2\{(\hat{\mathbf{u}}_k - b_k^u)^2 + (\hat{\mathbf{v}}_k - b_k^v)^2\}/B^2}. \tag{27}$$

$\hat{\mathbf{r}}_k, \hat{\mathbf{u}}_k, \hat{\mathbf{v}}_k$ are the MMSE estimates for r_k, u_k and v_k derived from $p(\mathbf{x}_k|\mathcal{Z}^k)$. Hence, α_k compensates both, the estimated positioning error of the radar beam and the propagation loss due to the radar equation. Assuming s_k to be constant, we have $\mathcal{I}_{\mu_{k|k}}\left(s_k;\, \hat{s}_{k|k-1}\right) = \mathcal{I}_{\mu_{k|k-1}}\left(s_k;\, \hat{s}_{k-1}\right)$. In principle, a dynamics regarding the cross section might be introduced.

1.4 Adaptive Sensor Control

Based on the previous considerations adaptive techniques for combined tracking and sensor management are discussed, i.e. control of data innovation intervals, radar beam positioning, and transmitted energy [17, 19].

1.4.1 Revisit Time Control

The time t_k of a radar allocation R_k is determined by the current lack of information conveniently described by the covariance matrix $\mathbf{P}_{k|k-1}$ of the predicted state estimate $\mathbf{x}_{k|k-1}$ [8]. Since the predicted pdf,

$$p(\mathbf{x}_k|\mathcal{Z}_{k-1}) = \sum_{\mathbf{i}_n^k} \boldsymbol{\mu}_{k|k-1}^{\mathbf{i}_n^k}\ \mathcal{N}(\mathbf{x}_k;\, \mathbf{x}_{k|k-1}^{\mathbf{i}_n^k},\, \mathbf{P}_{k|k-1}^{\mathbf{i}_n^k}), \tag{28}$$

is a normal mixture, we obtain:

$$\mathbf{P}_{k|k-1} = \sum_{\mathbf{i}_n^k} \boldsymbol{\mu}_{k|k-1}^{\mathbf{i}_n^k} \left(\mathbf{P}_{k|k-1}^{\mathbf{i}_n^k} + (\mathbf{x}_{k|k-1}^{\mathbf{i}_n^k} - \mathbf{x}_{k|k-1})\,(\mathbf{x}_{k|k-1}^{\mathbf{i}_n^k} - \mathbf{x}_{k|k-1})^\top\right). \tag{29}$$

The covariance of the individual mixture components the faster grow in time the more often maneuvers were assumed in the corresponding model histories. This has impact on the total covariance $\mathbf{P}_{k|k-1}$ according to the corresponding weighting factors. In addition $\mathbf{P}_{k|k-1}$ is "broadened" by the positive definite spread term. Evidently, the adaptive IMM modeling affects $\mathbf{P}_{k|k-1}$ in a rather complicated way. A scalar measure of the information deficit is provided by the largest eigenvalue of the covariance of the predicted target direction (in terms of u, v). Let it be denoted by $G_{k|k-1}$. A track update is allocated when the $G_{k|k-1}$ exceeds a predetermined proportion of the squared radar beam width B:

$$G_{k|k-1} > (v_0 B)^2. \tag{30}$$

The *relative track accuracy* v_0 introduced by this criterion is a measure of the minimum track quality required and a parameter to be optimized. In many practical applications $v_0 = 0.3$ is a reasonable choice [8].

1.4.2 Transmitted Energy

In view of the tracking system the sensor performance is mainly characterized by the signal-to-noise ratio that determines both, the detection probability and the measurement error. By suitably choosing the transmitted

energy per dwell e_k, the expected signal-to-noise ratio $\mathrm{SN}_{k|k-1}$ can be kept constant during tracking. Besides v_0, $\mathrm{SN}_{k|k-1}$ is an additional parameter subject to optimization. Since v_0 may be viewed as a measure of the beam positioning error, the energy e_k at time t_k is defined by this condition (Equation 8):

$$\mathrm{SN}_{k|k-1} \stackrel{!}{=} \text{const.} \tag{31}$$

$$\rightarrow \quad \frac{e_k}{e_0} = \left(\frac{\mathrm{SN}_0}{\mathrm{SN}_{k|k-1}}\right) \left(\frac{\bar{\sigma}_0}{\bar{\sigma}}\right) \left(\frac{\hat{\mathbf{r}}_{k|k-1}}{r_0}\right)^4 \mathrm{e}^{2v_0^2}. \tag{32}$$

By this particular choice the influence of the radar range equation is compensated (at least for a certain range interval). For the mean radar cross section $\bar{\sigma}$ either a worst-case assumption or estimates from target amplitude information can be used. Also the track quality v_0 affects the transmitted energy. As a side effect of this choice, the standard deviations $\sigma_k^{u,v}$ of the u, v-measurements are kept constant on an average.

1.4.3 BAYESian Local Search.

Intelligent algorithms for beam positioning and local search are crucial for IMM-type tracking. Too simple strategies may easily destroy the benefits of the adaptive dynamics model, because track loss immediately after a model switch is to be expected. For this reason the optimal approach based on the predicted densities $p(\mathbf{x}_k|\mathcal{Z}^{k-1})$ proposed in [8] is adopted to IMM tracking. The beam position of the first dwell is simply given by predicted direction $\hat{\mathbf{u}}_{k|k-1}$, $\hat{\mathbf{v}}_{k|k-1}$ derived from $p(\mathbf{x}_k|\mathcal{Z}^{k-1})$. If no detection occurs in the first dwell, however, this very result provides useful information on the target state. We thus have to calculate the conditional density given the event ¬D "no detection in this direction". BAYES' Rule yields:

$$p(u_k, v_k|\neg\mathrm{D}, \mathcal{Z}^{k-1}) \propto (1 - P_D(u_k, v_k))\, p(u_k, v_k|\mathcal{Z}^{k-1}) \tag{33}$$

up to a normalizing factor. In this density the detection probability P_D depends on the expected signal-to-noise ratio (Equation 8). By this the fluctuation model for the target RCS enters the discussion as it determines the functional forms of P_D (Equation 12). The two dimensional density $p(u_k, v_k|\neg\mathrm{D}, \mathcal{Z}^{k-1})$ can easily be calculated on a grid. The beam position for the next dwell is then simply provided by the maximum of $p(u_k, v_k|\neg\mathrm{D}, \mathcal{Z}^{k-1})$. This scheme is repeated until a detection occurs. Since the maximum is searched, the computation of the normalization integral is not required. Numerically efficient realizations are possible.

Figure 2 illustrates this scheme for one of the examples discussed below. First the predicted target pdf (a mixture) is shown as a function of its direction coordinates. With high probability the target is expected to be in the dark region, the true target position being indicated by a dark grey dot. The light dot denotes the beam position of the next dwell. The related detection probability is 26%. However, no detection occurred during the first dwell. We thus calculate the conditional pdf given that event. The resulting pdf differs significantly. The previous maximum decreased in height, while the global maximum is at a different location. Again no detection occurred; the resulting pdf is showed next. Now the algorithm decides to look again near the position at dwell 1. In addition, two smaller local maxima appear that increase in size at the next dwell as no detection occurred. We finally obtain a decision which leads to success. The last picture shows the updated pdf.

1.5 Discussion: Simulated Examples

Simulation results provide hints to what extend the total performance of multiple-target air surveillance by phased-array might be improved by using adaptive techniques for combined tracking and sensor control. Four questions are addressed:

1. Which resource savings (allocation time, energy) can be expected by using adaptive dynamics models?
2. How should the IMM dynamics modeling be designed (e.g. number of models, transition matrix)?

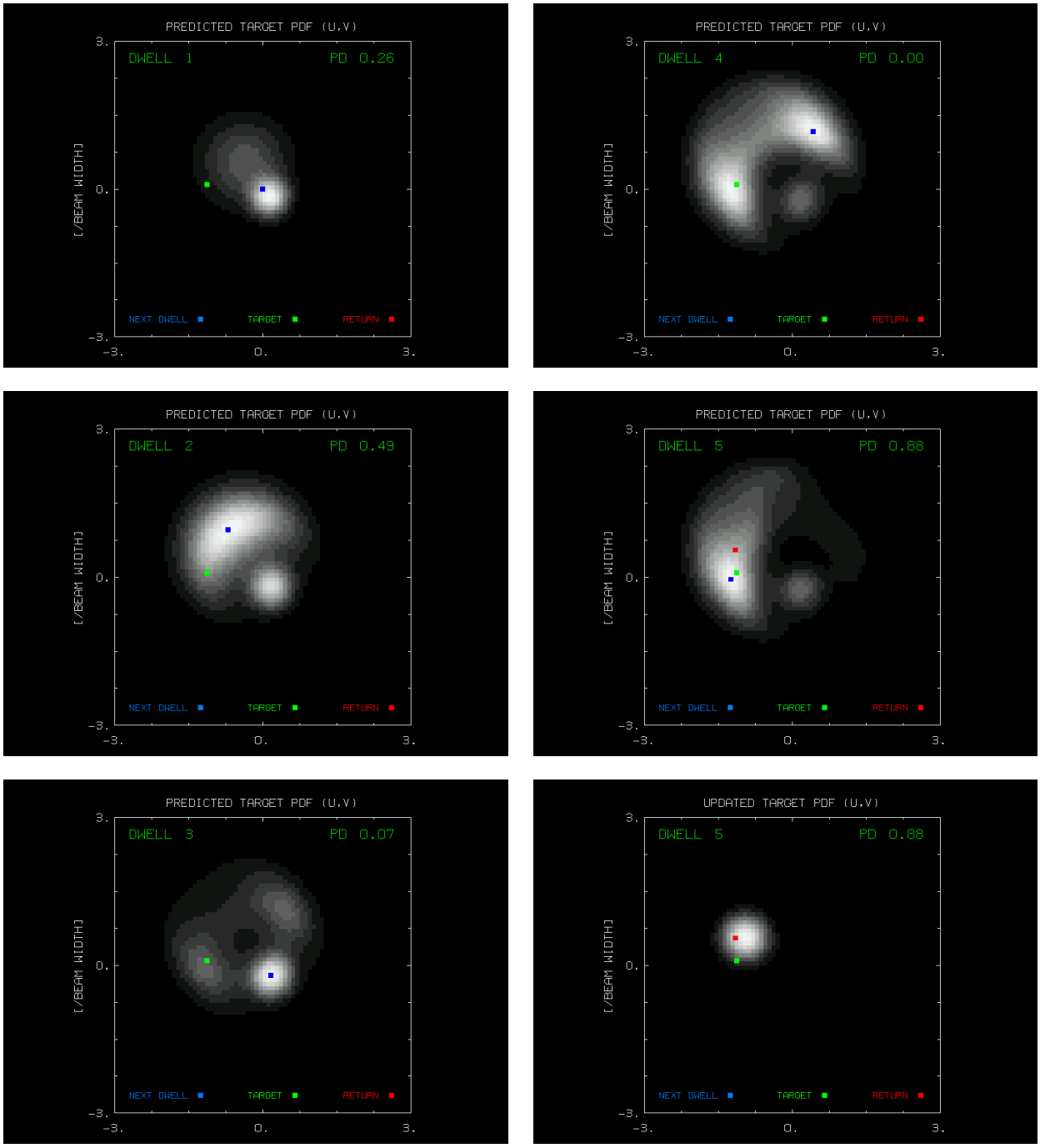

Figure 2: BAYESian local search: five consecutive dwells

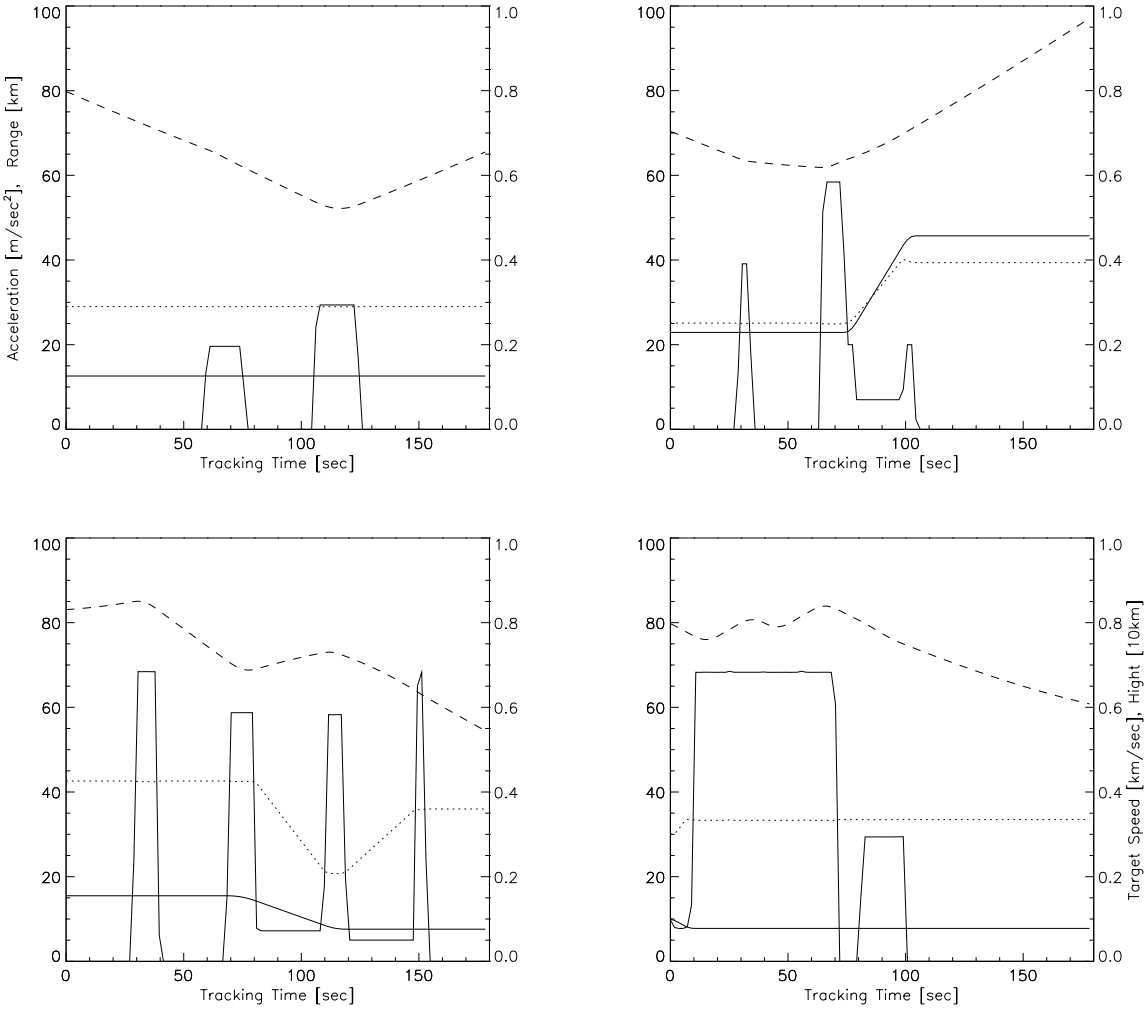

Figure 3: Horizontal projections and kinematical quantities

3. Which energy savings can be expected by exploiting target amplitude information for sensor control?

4. Why is BAYESian local search important when IMM dynamics models are used for revisit time control?

In general we follow the parameter and threshold settings recommended in[8]. To exclude false alarms due to receiver noise, the false alarm probability is $P_F = 10^{-4}$. False returns due to clutter or ECM are not considered. The error of range measurements (standard deviation) is $\sigma_r = 100$ m, the radar beam width $B = 1°$. We assume a minimum time interval of 20 ms between consecutive dwells on a particular target and statistically independent signal amplitudes (frequency decorrelation, e.g.). The reference range is set to $r_0 = 80$ km. Antenna coordinates (direction cosines, range) are used also for tracking; non-linearities introduced by these no-Cartesian coordinates are taken into account [7]. The maneuvering capability of the targets is thus characterized by two parameters: *maneuver correlation time* θ and *acceleration width* Σ. For $r = 2, 3$ we consider the parameter sets:

M_1 (worst-case model): $\Sigma_1 = 60$ m/s^2, $\theta_1 = 30$ s
M_2 (best-case model): $\Sigma_2 = 1$ m/s^2, $\theta_2 = 10$ s $\quad (p_{ij}) = \begin{pmatrix} .8 & .1 \\ .2 & .9 \end{pmatrix}$, $\quad (p_{ij}) = \begin{pmatrix} .8 & .1 & .0 \\ .0 & .9 & .2 \\ .2 & .0 & .8 \end{pmatrix}$.
M_3 (medium-case model): $\Sigma_3 = 30$ m/s^2, $\theta_3 = 30$ s

We observed that the performance does not critically depend on the particularly switching probabilities p_{ij} chosen. A detailed mismatch analysis, however, has not been performed. A track is considered to be lost if more than 50 dwells occur in the local search of if the beam positioning error Δb_k is greater than $3B$. We thus permit even a rather extensive local search that correspondingly burdens the total energy budget. In all simulations considered below (1000 runs) the relative frequency of track loss is less than 2%.

1.5.1 Benchmark Trajectories

The horizontal projection of four standard benchmark trajectories (military cargo aircraft, medium bomber, fighter/attack aircraft, and anti-ship missile) is shown in Figure 3 along with representative kinematical characteristics such as acceleration (solid line), range (dashed), height (dotted), and speed (solid). They have been proposed in [5, 6] and cover a rather wide range of militarily relevant targets. The missile trajectory might serve to explore the performance limits of the algorithms. In principle, missiles can execute even stronger maneuvers. It is questionable, however, if for those objects and their individual missions the dynamics models discussed above remain applicable. All targets are tracked over a period of 180 s. The RCS fluctuations are described by a Swerling-III model. The mean cross sections significantly vary from target to target (4., 2., 1.2, .5 m^2).

The discussion is confined to a few intuitively clear and simple performance measures obtained by Monte-Carlo simulation (1000 runs). In general a single performance measure is not sufficient as there may exist applications where the transmitted energy is the limiting factor, while in a different scenario the number of radar allocations must be kept low.

The adaptivity becomes visible if the performance is evaluated as a function of the tracking time that can be compared with the kinematics of the individual trajectories (Figure 3). Here we used histograms with 100 cells. In particular we considered: the mean revisit intervals, the mean number of dwells for a successful update, the mean number of sensor allocations totally required for track maintenance, the mean energy spent for a successful allocation, the mean energy totally spent for track maintenance, and the mean RCS of the targets estimated during tracking.

Four tracking filters were compared: worst-case KALMAN filter (KF), standard IMM filter with two or three models, respectively (S-IMM$_{2,3}$), and IMM-MHT filtering with model histories of length $n = 4$. For IMM-MHT with $n > 4$ the performance characteristics only slightly change. We thus conclude that $n = 4$ already provides a good approximation to optimal filtering (at least for the scenarios considered here). With reference to target amplitude information we considered three cases: 1) the target RCS $\bar{\sigma}$ is known and used for energy management. 2) The mean RCS $\bar{\sigma}$ is unknown and to be estimated during tracking. 3) A worst-case assumption is used for all targets ($\bar{\sigma} = 0.5$ m^2).

1.5.2 Design of IMM modeling

Practically, the question arises how many models should be used in the IMM approach. In addition it must be clarified if each trajectory needs an individual modeling or if the same IMM modeling can be used without significant loss of performance. For the fighter scenario a worst/best-case model should be appropriate at first sight. Trajectory 1 (Cargo Aircraft), however, shows that military targets can occur for which medium-case models are sufficient. To answer these questions we used IMM with two ($r = 2$, M_1, M_2) and three models ($r = 3$, M_1, M_2, M_3), respectively, with $v_0 = 0.3$, $\mathrm{SN}_{k|k-1} = 50$. In which way these parameters affect the performance is discussed further below. Figure 4 (first row) shows the resulting mean revisit intervals for all trajectories. The kinematical target characteristics are clearly mirrored. We observed:

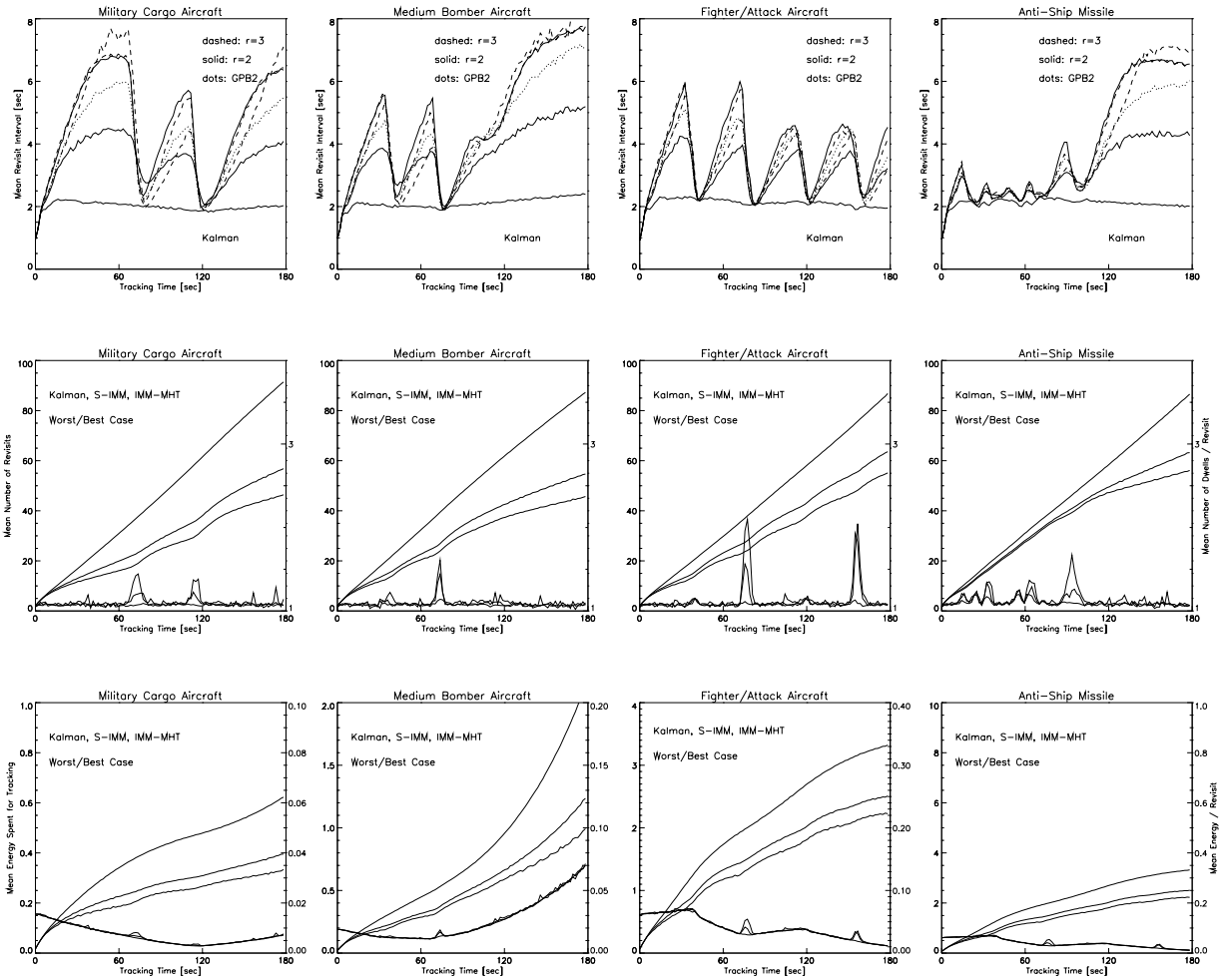

Figure 4: Revisit intervals, allocations, and energy for different filters and trajectories

1. As expected, KALMAN filtering ($r = 1$, M_1) leads to constant revisit intervals that are comparable for all trajectories. This is no longer true for S-IMM. The resultant curves related to $r = 2$ (solid) and $r = 3$ (dashed) significantly differ from each other. The onset of maneuvers (Figure 3) strongly affects the mean update intervals and thus illustrates the adaptivity of the algorithm.

2. The difference between the cases $r = 2, 3$ vanishes however, if IMM-MHT is used. If model histories are permitted (here $n = 4$), it seems to be irrelevant if besides worst/best-case assumption additional medium-case models are used. Even longer histories or further models ($r > 3$) do not significantly improve the performance obtained with $r = 2$ and $n = 4$. For a suitable (!) choice of the switching probabilities the performance of S-IMM$_4$ approaches closes to B-IMM$_2$; for B-IMM$_4$ no improvement over B-IMM$_2$ was observed.

3. For the bomber and the fighter S-IMM$_3$ (M_1, M_2, M_3) outperforms S-IMM$_2$ (M_1, M_2), in spite of the fact that for these trajectories worst-case maneuvers occur only and the medium-case model appeared to be unnecessary at first sight. The difference between $r = 2$ and $r = 3$, however, is not as clear as for scenario 1 (cargo aircraft).

4. For the moderately maneuvering cargo aircraft the question arises if the performance can be improved by using a medium/best-case IMM modeling. We found that worst/best-case IMM-MHT and medium/best-case IMM-MHT differ, but not very much. This indicates that worst/best-case IMM-MHT has a more or less "universal" character, i.e. it does not critically depend of the scenario considered (at least within certain limits).

These observations indicate that the mixtures $p(x_k|\mathcal{Z}^k)$ for $n = 4$, $r = 2$ have enough internal degrees of freedom to provide an adequate representation of the actual target behavior. Refined approximations by even more mixture components seem to be irrelevant for the trajectories considered. A Rule of thumb: A worst/best-case analysis of the problem along with IMM-MHT seems to be sufficient to achieve a nearly optimal tracking performance. Evidently, for two dynamics models reasonable and intuitive assumptions for the switching probabilities are easily obtained. IMM-MHT thus enables a more simplified dynamics modeling without significant loss of performance.

1.5.3 Gain by IMM modeling

For investigating the gain by adaptive dynamics models, let us for the present assume that the mean RCS of the target is known and used for energy management. Figure 4 shows the mean number of allocations required for track maintenance (KF, S-IMM$_2$, B-IMM$_2$). As expected, for KF the mean number of revisits linearly increases with increasing tracking time and is nearly the same for all trajectories. By adaptive dynamics modeling, however, the number of sensor allocations is reduced.

1. Compared with KF, IMM results in significant resource savings. There is an improvement by IMM-MHT over S-IMM; the difference, however, is less significant than between S-IMM and KF. Besides simplified modeling assumptions, the practical use of IMM-MHT therefore consists in the exploration of the limiting bounds for performance improvements.

2. The largest gain is observed for the cargo aircraft and the bomber. In case of the fighter the allocations required are reduced by about 50 % compared with worst-case KALMAN filtering. Even during the 7 g weaving of the missile some advantages of the IMM modeling can be observed.

Figure 4 (second row) also shows the mean number of dwells per revisit. Up to peaks corresponding with the onset of maneuvers, it is constant and roughly equal for all filters and trajectories. The peaks are the higher the more adaptivity the filter shows, i.e. the larger the revisit intervals can be during inertial flight.

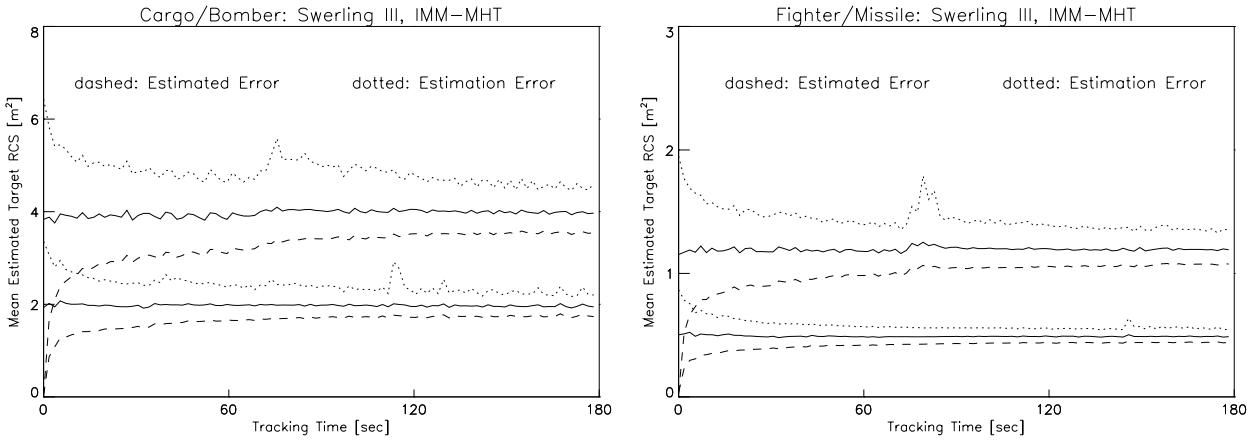

Figure 5: On the quality of RCS estimates

The peaks thus indicate that for abrupt maneuvers a local search might be required. This is the price to paid for increased adaptivity. Evidently, intelligent algorithms for beam positioning and local search are essential for IMM phased-array tracking.

These observations are consistent with Figure 4 (third row) which shows the mean energy spent for track maintenance (relative units). Besides the target maneuvers these curves are influenced also by the current target range (Figure 3, dotted line). In addition the mean energy spent per revisit is displayed. Up to characteristic peaks the energy per revisit is roughly the same for all tracking filters.

1.5.4 Quality of RCS Estimates

In a practical application the mean RCS of the targets to be tracked is unknown and might be estimated from target amplitude information. In general, the estimators used should be at least approximately bias-free, the estimated error and the empirical error should be roughly identical, and the estimators should show a certain robustness against model mismatch. As indicated by Figure 5, the estimator previously proposed provides rather satisfying results for all trajectories. Using IMM-MHT for tracking, the recursion was initiated with $\bar{\sigma} = .5$ m^2 (worst-case assumption) and $m_0 = 1.01$.

The solid lines show the mean RCS estimates as a function of the tracking time. For all scenarios it is roughly constant and corresponds with the actual values (4, 2, 1.2, 0.5 m^2). The dotted lines indicate the mean estimation error (available in the simulation). The curves show peaks that are related to the onset of maneuvers and the corresponding lack of track accuracy. The dashed lines denote the mean standard deviation calculated by the estimator itself. Tracking and RCS estimation are closely interrelated: Only when tracked over a certain period of time, estimates are reliable enough to distinguish between the target classes. A satisfying RCS estimation by signal processing only, i.e. without a temporal integration along the estimated trajectory does not seem to be possible. In this context IMM retrodiction techniques [16] might be considered which can provide more accurate estimates of the trajectory and thus more accurate RCS estimates.

1.5.5 RCS Model Mismatch

The backscattering properties of real targets are highly complex. A practicable method for estimating the RCS must thus show some robustness against model mismatch. To get a first hint, we generated in our

target type	processed	simulated	RCS [m^2]	estimated error	estimation error	energy
Bomber	III	III	1.96	0.22	0.28	0.37
	III	I	2.34	0.25	0.57	0.42
	I	III	1.77	0.28	0.33	0.39
	I	I	2.03	0.32	0.34	0.44
Fighter	III	III	1.19	0.13	0.16	0.82
	III	I	1.41	0.15	0.34	1.
	I	III	1.07	0.16	0.19	0.86
	I	I	1.22	0.18	0.19	0.99

Table 1: Mismatch regarding the fluctuation model

simulation amplitude information according to both Swerling I and III being processed according to both modeling assumptions. The results for the four possible combinations are summarized in table 1. Besides the quantities already shown in Figure 5, we also listed the total energy spent for tracking (relative units).

1. For matching models the RCS estimates are nearly bias-free and more or less roughly consistent.
2. For Swerling III fluctuations the estimates are more accurate than in case of Swerling I.
3. For Swerling I (no mismatch) more energy is spent than for Swerling III (keeping $SN_{k|k-1}$ constant).
4. If Swerling I amplitudes are processed according to Swerling III, the RCS is overestimated, consistency is lost.
5. It is underestimated if Swerling III amplitudes are processed according to Swerling I.
6. Mismatch does not greatly affect the performance (energy).

1.5.6 Energy Management

Finally we have to show up to what degree the radar energy to be spent can be reduced by estimating the RCS in comparison to worst-case assumptions. In Figure 5 the mean radar energy spent for track maintenance is displayed. The dotted lines refer to IMM-MHT tracking using the true RCS of the targets (as previously discussed). In a practical application this can not be realized; the resultant curves, however, may serve as a reference to discuss the performance of RCS-adaptive algorithms. The solid lines denote methods that exploit signal strength information for estimating the RCS (Worst-Case KALMAN filter, IMM-MHT). By dashed lines algorithms are indicated that use a worst-case assumption (here: 0.5 m^2, missile) on the RCS (KF, IMM-MHT).

A comparison between sensor control by using the true RCS (not available in a real application) and methods exploiting recursive RCS estimates is of particular interest. The largest deviation is observed for scenario 1 ($\bar{\sigma} = 4$ m^2). This is to be expected, as the recursion was started with a worst-case assumption. The discrepancy between both curves, however, is not very significant in all four cases. Compared with IMM-MHT (Worst-Case RCS) it can be neglected. The difference between sensor control with known and estimated RCS is roughly constant during tracking. We thus conclude that it is caused primarily in the initiation phase where not much signal strength information is yet available. As soon as reliable RCS estimates have been produced, the performance is practically identical. Figure 5 also shows how the resource savings due to adaptive dynamics models and RCS-adaptive energy management are related to each other.

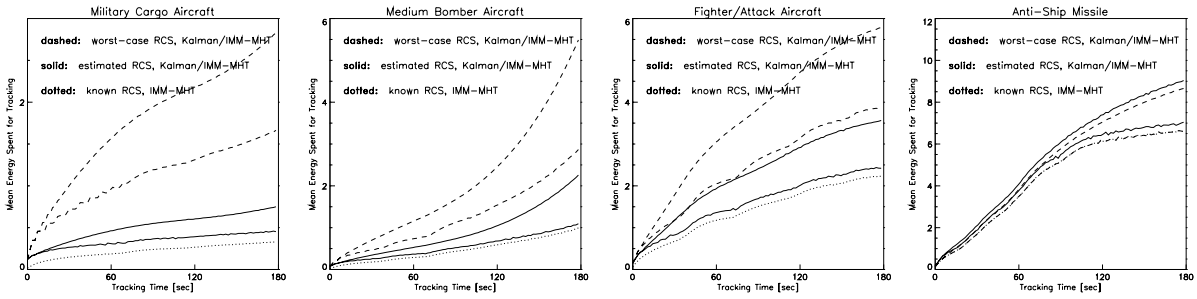

Figure 6: Mean Number of Allocations for Different Filters and Trajectories

target type	RCS	filter	ΔT [s]	revisits	energie	rel.
Cargo	worst case	KALMAN	3.3	55.1	2828	8.5
		IMM-MHT	6.5	32.6	1664	5.0
	estimated	KALMAN	2.0	90.3	750	2.2
		IMM-MHT	4.9	45.0	453	1.4
	known		4.9	46.4	334	1
Bomber	worst case	KALMAN	3.1	60.1	5488	5.5
		IMM-MHT	6.4	34.0	2868	2.9
	estimated	KALMAN	2.2	85.5	2257	2.3
		IMM-MHT	5.1	44.2	1095	1.1
	known		5.0	45.7	993	1
Fighter	worst case	KALMAN	2.8	67.3	5786	2.6
		IMM-MHT	4.9	43.3	3882	1.7
	estimated	KALMAN	2.2	85.6	3563	1.6
		IMM-MHT	3.9	54.0	2420	1.1
	known		3.8	55.1	2226	1
Missile	worst case	KALMAN	2.1	86.6	8657	1.3
		IMM-MHT	4.1	56.1	6593	1
	estimated	KALMAN	2.2	85.4	9036	1.4
		IMM-MHT	4.2	55.4	7042	1.1
	known		4.1	56.1	6593	1

Table 2: Gain by RCS-adaptive energy control

In table 2 for all scenarios and processing methods scalar performance measures are summarized: target revisit intervals (ΔT), sensor allocations required, energy spent for track maintenance (time averages taken over the tracking time). The last column shows the energy spent by the various methods relative to IMM-MHT with known RCS. Compared with IMM-MHT (Worst-Case RCS) the gain is: 3.8 (cargo aircraft), 2.6 (Bomber), 1.5 (Fighter), .9 (anti-ship missile). Hence, in the missile-scenario, where the worst-case assumption is correct, a small loss of performance must be taken into account.

2 Sensor Fusion for Ground Target Tracking

Ground surveillance aims at near real-time production of a dynamic ground picture. This task comprises track extraction and track maintenance of single ground moving vehicles and convoys, mobile weapon systems or military equipment, as well as low-flying targets such as helicopters. As ground target tracking is a challenging problem all available information sources must be exploited, i.e. the sensor data themselves as well as background knowledge about the sensor performance and the underlying scenario.

For long-range, wide-area, all-weather, and all-day ground surveillance operating at high data update rates, GMTI radar proves to be the sensor system of choice (GMTI: Ground Moving Target Indication). By using airborne sensor platforms in stand-off ground surveillance applications the effect of topographical screening is alleviated, thus extending the sensors' field of view. In [12] characteristic problems of signal processing related to GMTI tracking with STAP radar are discussed. We here discuss selected tracking aspects, which arise from using more appropriate sensor models and expoiting background information. The following topics are of particular interest:

- *Doppler-Blindness.* Even after platform motion compensation by using STAP techniques [13], ground moving vehicles can well be masked by the clutter notch of the sensor. This physical phenomenon directly results from the low-Doppler characteristics of ground moving vehicles and causes interfering fading effects that seriously affect track accuracy and track continuity. Unless appropriately handled, Doppler-blindness can cause serious problems, which seem to be even more difficult in the presence of Doppler ambiguities.

- *Road-Map Information.* Even military targets usually move on road networks, whose topographical coordinates are known in many cases. Digitized topographical road maps such as provided by Geographical Information Systems (GIS) should therefore enter into the target tracking and sensor data fusion process. The problem of battlefield surveillance is not considered here (i.e. off-road targets).

- *Sensor Data Fusion.* Since a single GMTI sensor on a moving airborne platform can record the situation of interest merely over short periods of time, sensor data fusion proves to be of particular importance. The data processing and fusion algorithms used for ground surveillance are closely related to the statistical, logical, and combinatorial methods applied to air surveillance.

A GMTI radar sensor produces measurements of kinematical target parameters and possibly false returns caused by residual clutter, e.g.. In addition, measurement errors and sensor parameters are provided. The resulting tracks represent the kinematical states of the targets along the corresponding accuracies and as such are prerequisites for producing a ground picture. We here discuss track maintenance for well-separated vehicles in case of low residual clutter.

The papers [9, 10] are the standard references explicitly devoted to the problem of GMTI tracking with single and multiple sensors. The impact of sensor modeling on GMTI tracking is is discussed in [18].

2.1 Discussion of an idealized Scenario

Assuming a flat earth Figure 7 shows an idealized scenario with two airborne GMTI sensors observing a ground vehicle moving with constant speed (15 m/s = 54 km/h) parallel to the x-axis for most of the time. This situation is typical of stand-off or gap-filling ground surveillance missions. In the second half of the observation period over $\Delta t_{\max} = 25$ min the target stops for 7 min. Then it speeds up again reaching its initial velocity. Finally, the target leaves the field of view of sensor 2.

In Table 1 selected sensor and platform parameters are summarized. h_p, v_p denote the constant height and speed of the sensor platforms over ground. Δr, $\Delta\varphi$ are the range and azimuth regions covered by each sensor during observation. The revisit intervals are given by ΔT, while MDV denotes the Minimum Detectable Velocity, a GMTI-specific sensor parameter being important to ground moving target tracking.

Sensor	h_p [km]	v_p [m/sec]	Δr [km]	$\Delta\varphi$ [deg]	ΔT [sec]	MDV [m/sec]
1	10	200	[232, 292]	[-128, -67]	15	2
2	1	40	[22, 54]	[77, 172]	10	2

Table 3: selected sensor and platform parameters

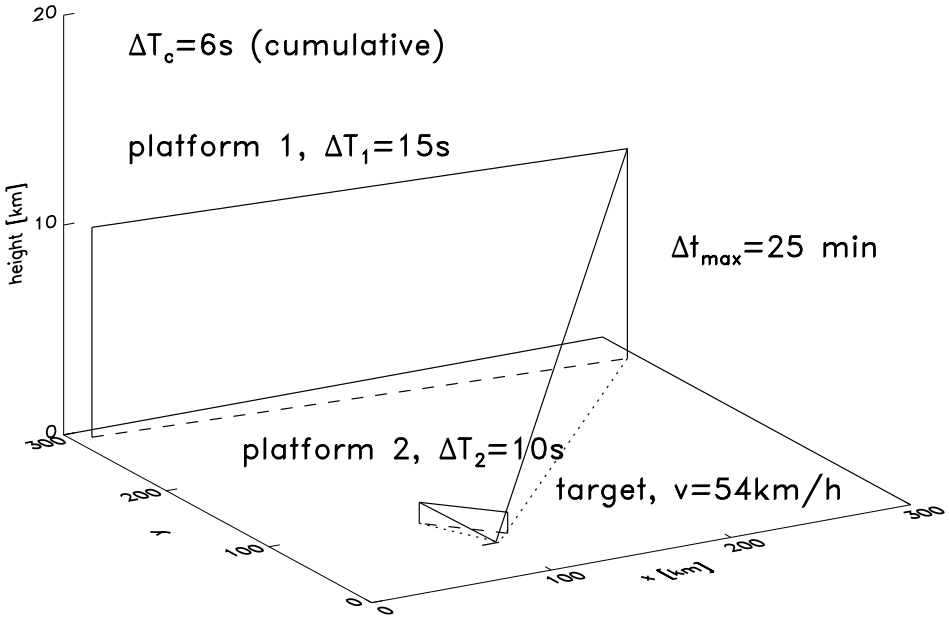

Figure 7: simplified scenario

2.1.1 Doppler-Blindness

Even after platform motion compensation by using STAP-techniques [13], GMTI tracking may remain a difficult task. Unless appropriately handled, in particular two phenomena can cause problems:

1. Sensor-to-target geometries can occur where targets to be tracked are masked by the clutter notch of the sensor. This results in a series of missing detections until the geometry is changing again.

2. As stopping targets are indistinguishable from ground clutter, the early detection of a stopping event itself as well as tracking of ‘stop & go’ targets can be important to military applications.

The impact of these effects on the detection probability is shown in Figure 8 for the scenario previously introduced. For both sensors we observe deep notches (dashed line: platform 1, dotted line: platform 2). In the center of these notches the radial velocities of the target and the surrounding ground patch are very close to each other, thus making target discrimination by Doppler processing (STAP [13]) impossible. This is particularly true if the target stops.

The dashed and solid lines in Figure 9 denote the radial velocities of ground patches around the target and target returns, respectively. The area shaded in grey reflects the width of the clutter notchs of the sensors, which is determined by the individual Minimum Detectable Velocities (MDVs). For each sensor both curves

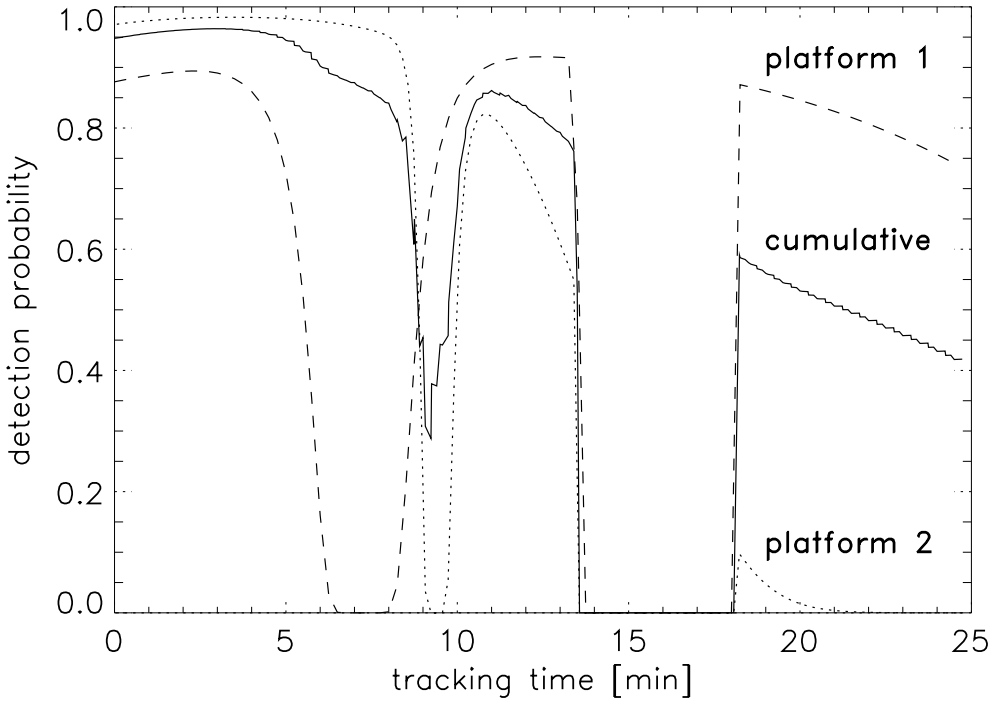

Figure 8: detection probability

are closely adjacent to each other indicating that the target is moving at a much lower speed than the sensor platforms. We notice sliding intersections between the curves. They are responsible for the relatively long duration of Doppler-blind phases.

2.1.2 GMTI Model

For dealing with this phenomenon we propose a refined model for describing the sensor characteristics and discuss its benefits for improving the performance of ground target tracking and sensor data fusion. The model is adapted to STAP techniques in that the detection probability assumed in the tracking process is described as a function of the GMTI-specific clutter notch. While the current location of the notch is determined by the kinematical state of the target and the current sensor-to-target geometry, its width is given by a characteristic sensor parameter (MDV).

By this more detailed information on the sensor performance can be incorporated into the tracking process. This in particular permits a more appropriate treatment of missing detections. In other words, information on the potential reasons that might have caused the missing detections enters into the tracking filter. We observed that by this measure the number of lost tracks can significantly be reduced while the track continuity is improved, finally leading to a more reliable ground picture.

2.1.3 Sensor Fusion

Assuming an idealized processing architecture (centralized data fusion), the *mean cumulative revisit interval* ΔT_c results from the individual revisit intervals ΔT_i, $i = 1, \ldots, n_s$, of n_s sensors according to

$$\frac{1}{\Delta T_c} = \sum_{i=1}^{n_s} \frac{1}{\Delta T_i}. \tag{34}$$

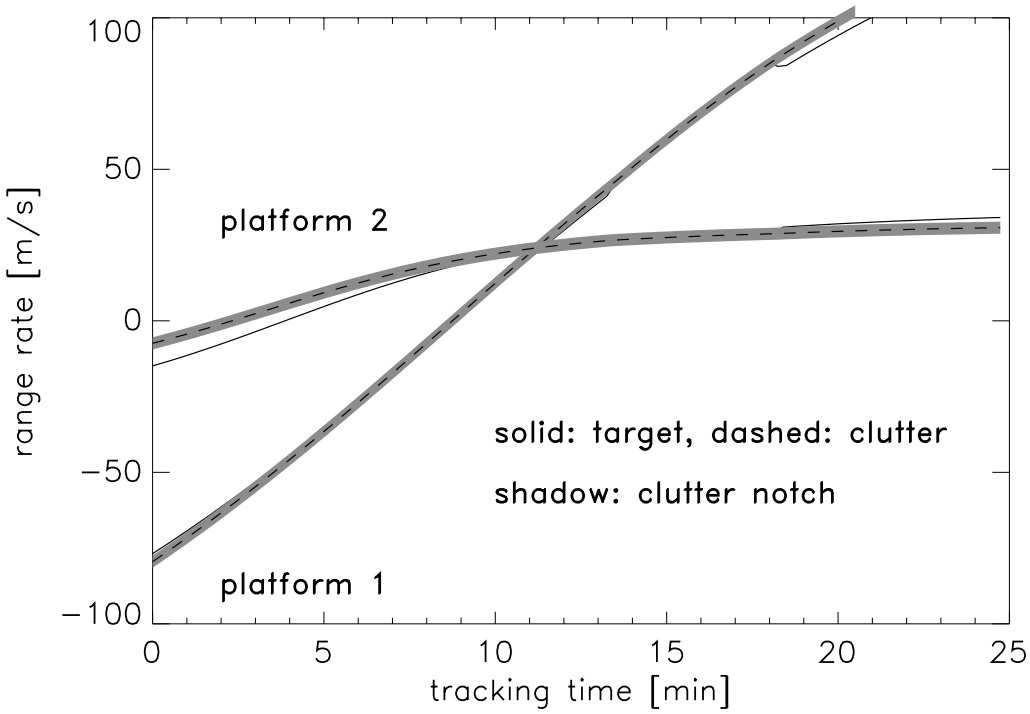

Figure 9: range rate (ground, target)

For the previous example ($n_s = 2$, $\Delta T_1 = 15$ s, $\Delta T_2 = 10$ s) we obtain $\Delta T_c = 6$ s. The *mean cumulative detection probability* P_D^c referring to ΔT_c is given by

$$P_D^c = 1 - \prod_{i=1}^{n_s} (1 - P_D^i)^{\frac{\Delta T_c}{\Delta T_i}} \tag{35}$$

with P_D^i denoting the detection probabilities of the individual sensors, which depend on the corresponding sensor-to-target geometries. Evidently, the corresponding revisit intervals ΔT_i also enter into this formula, which describes the mean improvement of the overall detection performance to be expected by sensor data fusion. The larger the individual revisit interval ΔT_i of sensor i, the smaller is the effect of sensor i on the collective performance, even if the corresponding individual detection probability P_D^i is large. ΔT_c and P_D^c are averaged quantities, by which the expected performance improvement can be predicted in an overall sense.

Figure 9 shows the mean cumulative detection probability P_D^c for the above example (solid line). The impact of the clutter notches are more or less compensated. Due to the fact that P_D^c is related to the mean cumulative revisit interval $\Delta T_c = 6$ s, being shorter than those of the individual sensors ($\Delta T_1 = 10$ s, $\Delta T_2 = 15$ s), P_D^c is smaller than the detection probability of the sensor dominating at that time.

2.2 Tracking Preliminaries

The choice of a suitable coordinate system for describing the underlying sensor/target geometry, the sensor platform trajectory, and the available a priori information on the dynamical behavior of ground moving targets are prerequisites to target tracking.

2.2.1 Coordinate Systems

For the sake of simplicity we consider three coordinate systems in which the underlying physical phenomena become transparent:

1. Cartesian *ground* coordinates, where the description of the target and platform kinematics is of a particularly simple form,
2. the moving Cartesian *antenna* coordinate system, whose x-axis is oriented along the array antenna of the GMTI radar mounted on the airborne sensor platform,
3. the *sensor* coordinate system, in which the measurements of the kinematical target parameters are described (target range, azimuth, and range-rate).

Furthermore a flat earth is assumed. In the applications the use of coordinates different from those may be more convenient.

Antenna Coordinates. In ground coordinates the kinematical state $\mathbf{x}_p(t)$ of a platform moving at a constant height h_p and a constant velocity $\dot{\mathbf{r}}_p = v_p(\cos\varphi_p, \sin\varphi_p, 0)^\top$ is given by $\mathbf{x}_p(t) = (\mathbf{r}_p(t), \dot{\mathbf{r}}_p)^\top$ with $\mathbf{r}_p(t) = \mathbf{r}_p(0) + \dot{\mathbf{r}}_p\, t$ and $\mathbf{r}_p(0) = (x_p, y_p, h_p)^\top$. Let the orientation of the antenna array relative to the platform velocity $\dot{\mathbf{r}}_p$ be defined by the direction vector $\mathbf{e}_a = (\cos\varphi_a, \sin\varphi_a, 0)^\top$. The cases $\varphi_a = 0, \pi/2$ describe side- and forward-looking array antennas, respectively (SLAR/FLAR). Due to aircraft crab, however, even in case of side-looking antennas $\varphi_a \neq 0$ may occur (crab angle). The transforms $\mathbf{x}_k^a = \mathbf{t}_{g\leftarrow a}[\mathbf{x}_k^g; t_k]$, $\mathbf{x}_k^g = \mathbf{t}_{a\leftarrow g}[\mathbf{x}_k^a; t_k]$ between the kinematical states $\mathbf{x}_k^g$, $\mathbf{x}_k^a$ in ground/antenna coordinates at time t_k, respectively, are given by:

$$\mathbf{t}_{a\leftarrow g}[\mathbf{x}_k^g; t_k] = \mathbf{T}_{a\leftarrow g}\left[\mathbf{x}_k^g - \mathbf{x}_p(t_k)\right] \tag{36}$$

$$\mathbf{t}_{g\leftarrow a}[\mathbf{x}_k^a; t_k] = \mathbf{T}_{g\leftarrow a}\mathbf{x}_k^a + \mathbf{x}_p(t_k) \tag{37}$$

with $\mathbf{T}_{a\leftarrow g} = \mathbf{T}_{g\leftarrow a}^\top$ and $\mathbf{T}_{g\leftarrow a}$ given by:

$$\mathbf{T}_{g\leftarrow a} = \begin{pmatrix} \mathbf{R}_z(\varphi_p - \varphi_a) & 0 \\ 0 & \mathbf{R}_z(\varphi_p - \varphi_a) \end{pmatrix}, \quad \mathbf{R}_z(\varphi) = \begin{pmatrix} \cos\varphi & \sin\varphi & 0 \\ -\sin\varphi & \cos\varphi & 0 \\ 0 & 0 & 1 \end{pmatrix}.$$

Sensor Coordinates. Let $\mathbf{x}_k^a = (\mathbf{r}_k^a, \dot{\mathbf{r}}_k^a)^\top$ with $\mathbf{r}_k^a = (x_k, y_k, -h_p)^\top$ and $\dot{\mathbf{r}}_k^a = (\dot{x}_k, \dot{y}_k, 0)^\top$ denote the kinematical target state in antenna coordinates and let $\mathbf{x}_k = (r_k, \varphi_k, \dot{r}_k, \dot{\varphi}_k)^\top$ be the corresponding quantity in sensor coordinates. The non-linear transforms between both coordinate systems are given by:

$$\mathbf{t}_{s\leftarrow a}[\mathbf{x}_k^a] = \left(\sqrt{x_k^2 + y_k^2 + h_p^2},\ \arctan\frac{y_k}{x_k},\ \frac{x_k\dot{x}_k + y_k\dot{y}_k}{\sqrt{x_k^2 + y_k^2 + h_p^2}},\ \frac{x_k\dot{y}_k - \dot{x}_k y_k}{x_k^2 + y_k^2} \right)^\top \tag{38}$$

$$\mathbf{t}_{a\leftarrow s}[\mathbf{x}_k] = \sqrt{r_k^2 - h_p^2}\left(\cos\varphi_k,\ \sin\varphi_k,\ -h_p, \right.$$
$$\left. \frac{r_k\dot{r}_k\cos\varphi_k}{r_k^2 - h_p^2} - \dot{\varphi}_k\sin\varphi_k,\ \frac{r_k\dot{r}_k\sin\varphi_k}{r_k^2 - h_p^2} + \dot{\varphi}_k\cos\varphi_k,\ 0 \right)^\top. \tag{39}$$

The transforms between ground and sensor coordinates, $\mathbf{t}_{s\leftarrow g}[\mathbf{x}_k^g; t_k]$, $\mathbf{t}_{g\leftarrow s}[\mathbf{x}_k; t_k]$, result from the concatenation of these transforms. The calculation of the related JACOBIans, $\mathbf{T}_{s\leftarrow g}[\mathbf{x}_k^g] = \partial\mathbf{t}_{s\leftarrow g}/\partial\mathbf{x}_k^g$ and $\mathbf{T}_{g\leftarrow s}[\mathbf{x}_k] = \partial\mathbf{t}_{g\leftarrow s}/\partial\mathbf{x}_k$, is straightforward.

2.2.2 Target Dynamics

Let the kinematical state vector of a ground moving target at time t_k be given by its current position $\mathbf{r}_k^g = (x_{k;1}^g, x_{k;2}^g, x_{k;3}^g)^\top$ and velocity $\dot{\mathbf{r}}_k^g$:

$$\mathbf{x}_k^g = (\mathbf{r}_k^g, \dot{\mathbf{r}}_k^g)^\top = (x_{k;1}^g, \ldots, x_{k;6}^g)^\top. \tag{40}$$

Due to the small agility of ground targets, acceleration components are omitted. In the previous scenario (Figure 7) we in particular have: $x_{k;3}^g = x_{k;6}^g = 0$.

Cartesian Coordinates. In the ground coordinate system the target dynamics is modeled by a linear system equation with additive white GAUSSian noise. With the quantity $\Sigma_{k|k-1} = v_t(1-\mathrm{e}^{-2(t_k-t_{k-1})/\theta_t})^{1/2}$ (discussed below), 3D diagonal matrices $\mathbf{J} = \mathrm{diag}[1,1,0]$, $\mathbf{O} = \mathrm{diag}[0,0,0]$, and $\mathbf{v}_k \sim N(0,\mathbf{J})$, a realization close to the model in the first talk (subsection 2.2.1):

$$\mathbf{x}_k^g = \mathbf{F}_{k|k-1}^g \mathbf{x}_{k-1}^g + \mathbf{G}_{k|k-1}^g \mathbf{v}_k \tag{41}$$

with matrices $\mathbf{F}_{k|k-1}^g$ and $\mathbf{G}_{k|k-1}^g$ given by:

$$\mathbf{F}_{k|k-1}^g = \begin{pmatrix} \mathbf{J} & (t_k - t_{k-1})\mathbf{J} \\ \mathbf{O} & \mathrm{e}^{-(t_k-t_{k-1})/\theta_t}\mathbf{J} \end{pmatrix}, \quad \mathbf{G}_{k|k-1}^g = \Sigma_{k|k-1}\begin{pmatrix} \mathbf{O} \\ \mathbf{J} \end{pmatrix}. \tag{42}$$

The modeling parameters v_t (*limiting speed*) and θ_t (*maneuver correlation time*) in $\Sigma_{k|k-1}$ have a clear meaning. In contrast to the dynamics model used in [9], the model naturally introduces a 'speed limit' v_t, while θ_t may characterize different target types.

Sensor Coordinates. With the non-linear transforms $\mathbf{t}_{g\leftarrow s}$, $\mathbf{t}_{s\leftarrow g}$ between ground and sensor coordinates, a first-order Taylor expansion around $\mathbf{x}_{k-1|k-1}^g$ and $\mathbf{x}_{k-1|k-1}$ (the state estimates at t_{k-1} in ground and sensor coordinates, respectively, using all associated measurements up to and including t_{k-1}) yields a linearized system equation in the moving sensor coordinate system:

$$\mathbf{x}_k = \mathbf{F}_{k|k-1}\mathbf{x}_{k-1} + \mathbf{G}_{k|k-1}\mathbf{v}_k + \mathbf{u}_{k|k-1} \tag{43}$$

where:

$$\begin{aligned} \mathbf{F}_{k|k-1} &= \mathbf{T}_{s\leftarrow g}[\mathbf{x}_{k|k-1}^g]\mathbf{F}_{k|k-1}^g\mathbf{T}_{g\leftarrow s}[\mathbf{x}_{k-1|k-1}], \quad \mathbf{G}_{k|k-1} = \mathbf{T}_{s\leftarrow g}[\mathbf{x}_{k|k-1}^g]\mathbf{G}_{k|k-1}^g \\ \mathbf{u}_{k|k-1} &= \mathbf{f}_{k|k-1}[\mathbf{x}_{k-1|k-1}] - \mathbf{F}_{k|k-1}\mathbf{x}_{k-1|k-1}, \quad \mathbf{x}_{k|k-1}^g = \mathbf{F}_{k|k-1}^g\mathbf{t}_{g\leftarrow s}[\mathbf{x}_{k-1|k-1}; t_{k-1}] \\ \mathbf{f}_{k|k-1}[\mathbf{x}_{k-1|k-1}] &= \mathbf{t}_{s\leftarrow g}[\mathbf{F}_{k|k-1}^g\mathbf{t}_{g\leftarrow s}[\mathbf{x}_{k-1|k-1}; t_{k-1}]; t_k]. \end{aligned}$$

2.3 GMTI Sensor Model

In the subsequent considerations $Z_k = \{\mathbf{z}_k^i\}_{n=0}^{n_k}$ denotes a set of n_k sensor reports (frame of observations), which are detected at time t_k (revisit time). In this notation let $\mathbf{z}_k^0$ be the event that at time t_k the sensor possibly produced no valid target detection.

2.3.1 GMTI Chacteristics

Due to the physical and technical reasons previously discussed, the detection of ground moving targets by airborne radar is limited by strong ground clutter returns. This can be much alleviated by STAP techniques [13]. The characteristics of STAP processing, however, directly influence the GMTI tracking performance.

Main-Lobe Clutter. Let us consider a ground patch located at the position $\mathbf{r}_c^g$ in ground coordinates (i.e. $\dot{\mathbf{r}}_c^g = \mathbf{o}$), which is illuminated by the main-lobe of the moving STAP radar sensor. In antenna coordinates let r and φ denote slant range and azimuth angle of the ground patch related to the Cartesian position vector $\mathbf{r}_c^a = \sqrt{r^2 - h_p^2}\,(\cos\varphi, \sin\varphi, 0)^\top$. According to Equation 36 in the moving antenna coordinate system the state vector of the ground patch is given by $\mathbf{x}_c^a = (\mathbf{r}_c^a, \dot{\mathbf{r}}_c^a)^\top$ with a non-zero velocity vector $\dot{\mathbf{r}}_c^a = -v_p(\cos\varphi_a, \sin\varphi_a, 0)^\top$. The radial velocity of the ground patch therefore directly results from equation 39:

$$\dot{r}_c(r, \varphi; v_p, h_p, \varphi_a) = -v_p \cos(\varphi - \varphi_a) \sqrt{1 - (h_p/r)^2}. \tag{44}$$

Besides the location of the ground patch described by r and φ the radial velocity $\dot{r}_c$ depends on the parameters platform speed v_p, platform height h_p, and the orientation of the antenna with respect to the flight direction φ_a.

For physical and technical reasons the signal processing for airborne GMTI radar [13] is unable to separate a ground moving target from the surrounding main-lobe clutter return if the target's radial velocity is equal to $\dot{r}_c$, i.e., if its kinematical state vector $\mathbf{x}_k = (r_k, \varphi_k, \dot{r}_k, \dot{\varphi}_k)^\top$ of the target obeys the relation $n_c(\mathbf{x}_k) = 0$ where the function n_c is given by:

$$n_c(\mathbf{x}_k) = n_c(r_k, \varphi_k, \dot{r}_k; v_p, h_p, \varphi_a) \tag{45}$$

$$= \dot{r}_k - \dot{r}_c(r_k, \varphi_k; v_p, h_p, \varphi_a). \tag{46}$$

In other words, the equation $n_c(\mathbf{x}_k) = 0$ defines the location of the GMTI-specific clutter notch of the sensor in the state space of a ground target and as such reflects a fundamental physical/technical fact without implying any further modeling assumptions.

Qualitative Discussion. An adequate modeling of this phenomenon is important to ground moving target tracking. Besides being simple enough to be mathematically tractable, the GMTI sensor model must reflect the following qualitative conclusions:

1. The detection probability of the sensor depends on the kinematical target state and the sensor/target geometry: $P_D = P_D(\mathbf{x}_k)$.
2. $P_D(\mathbf{x}_k)$ is small in a certain region $|n_c(\mathbf{x}_k)| <$ MDV around the clutter notch characterized by the sensor parameter MDV.
3. Far from the clutter notch, the detection probability depends only on the directivity pattern of the sensor and the target range.
4. There exists a comparatively narrow transient region between these two domains in the state space of the ground target.

Quantitative Modeling. In a generic description of the detection performance of GMTI sensors it seems plausible to write $P_D = P_D(\mathbf{x}_k)$ as a product with one factor reflecting the directivity pattern and propagation effects due to the radar equation [3], $p_D = p_D(r_k, \varphi_k)$, the other factor being related to the clutter notch. To this end, let us consider functions of the following form:

$$P_D(r_k, \varphi_k, \dot{r}_k) = p_d(r_k, \varphi_k) \left(1 - \mathrm{e}^{-\frac{1}{2}\left(\frac{n_c(r_k, \varphi_k, \dot{r}_k)}{\mathrm{MDV}}\right)^2}\right). \tag{47}$$

In this expression the sensor parameter MDV has a clear and intuitive meaning: In the region defined by $|n_c(\mathbf{x}_k)| <$ MDV we have $P_D < \frac{1}{2}\, p_d$. The parameter MDV is thus a quantitative measure of the minimum

radial velocity with respect to the sensor platform which a ground moving target must at least have to be detected by the sensor (Minimum Detectable Velocity). The actual size of MDV depends on the particular signal processor used.

For SWERLING I targets p_d is given by: $p_d(r,\varphi) = {p_F}^{1/[1+\mathrm{snr}(r,\varphi)]}$ with the false alarm probability p_F and the signal-to-noise ratio $\mathrm{snr}(r,\varphi) = \mathrm{snr}_0\ D(\varphi)\ (\sigma/\sigma_0)\ (r/r_0)^{-4}$ according to [3]. Let the sensor's directivity pattern be described by $D(\varphi) = \sin^2(\varphi - \varphi_a)$.

2.3.2 Convoi Resolution

Since in military ground traffic vehicles often move in convoys, at first view resolution phenomena seem to be typical of long-range ground surveillance. Due to the asymmetric effect of range and angle resolution, however, Doppler-blindness in many cases superimposes resolution effects: As soon as convoy targets cease to be resolvable, they are at the same time buried in the clutter notch and thus escape detection. Vice versa, resolvable convoy targets are rarely Doppler-screened. A separate modeling of the sensor resolution might therefore be omitted.

As an example we assume two targets moving in a row along a straight road with 30 km/h as typical of military applications. Their mutual distance is 50 m. The target/sensor geometry is as depicted in Figure 7. Let the sensor resolution be given by: $\alpha_r = 10$ m (range), $\alpha_\varphi = 0.1°$ (azimuth), $\alpha_{\dot r} = 0.5$ m/s (range-rate). Figure 10 shows the detection probabilities of both sensors (solid lines). The width of the notches is larger than in Figure 8 due to the smaller convoy speed. The dotted lines denote the resolution probabilities P_r of the sensors modeled according to the discussion in the previous talk (subsection 3.2.3):

$$P_r = 1 - e^{-\log 2(\Delta r/\alpha_r)^2}\ e^{-\log 2(\Delta\varphi/\alpha_\varphi)^2}\ e^{-\log 2(\Delta\dot r/\alpha_{\dot r})^2}. \tag{48}$$

Δr, $\Delta\varphi$, $\Delta\dot r$ are the distances between the targets in sensor coordinates. If P_r is dominated by the angular resolution (i.e. Δr and $\Delta\dot r$ are small), Doppler-blindness occurs. Outside of the notch the high range/range-rate resolution guarantees resolved returns. For an approach to track ground moving convoys see [15].

2.4 GMTI Data Processing

According to BAYES' formula, the processing of the new sensor data Z_k received at time t_k makes use of the predicted density $p(\mathbf{x}_k|\mathcal{Z}^{k-1})$ (previously calculated) and the measurement likelihood function $p(Z_k, n_k|\mathbf{x}_k)$.

2.4.1 Likelihood Function

The likelihood function $p(Z_k, n_k|\mathbf{x}_k)$ statistically describes what a single frame of reports $Z_k = \{\mathbf{z}_k^i\}_{n=0}^{n_k}$ at time t_k can say about the target state $\mathbf{x}_k$. Its particular structure is determines by the current sensor data frame and the sensor model describing the sensor's properties. The likelihood function can be written as a sum over all interpretation hypotheses regarding the origin of the data. For well-separated targets in a possibly cluttered environment two classes of data interpretations can be identified:

1. The object being considered was not detected, the received sensor data are false.
2. The target was detected, $\mathbf{z}_k^i$ is the target measurement, all other returns are false.

For the sake of simplicity let us first consider Doppler-unambiguous measurements. According to the previous modeling assumptions we obtain up to a factor, which is independent of $\mathbf{x}_k$ and the measurements (see the discussion in the previous talk, subsection 3.3.1), the following expression:

$$p(Z_k, n_k|\mathbf{x}_k) \propto \big(1 - P_D(\mathbf{x}_k)\big)\rho_F + P_D(\mathbf{x}_k) \sum_{n=1}^{n_k} \mathcal{N}\big(\mathbf{z}_k^n;\ \mathbf{H}\mathbf{x}_k,\ \mathbf{R}\big) \tag{49}$$

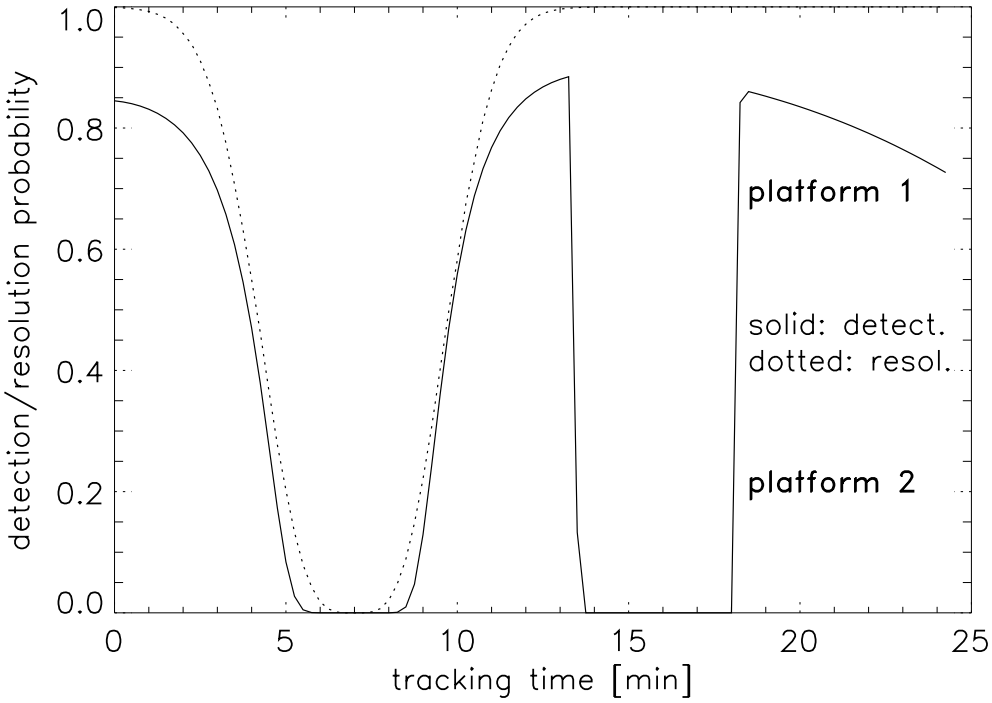

Figure 10: detection and resolution probability

with ρ_F denoting the spatial false return density. In this expression the function $n_c(\mathbf{x}_k)$ in the definition of the detection probability $P_D(\mathbf{x}_k)$ (equation 47) is linearized around the predicted state estimate $\mathbf{x}_{k|k-1} = (r_{k|k-1}, \varphi_{k|k-1}, \dot{r}_{k|k-1}, \dot{\varphi}_{k|k-1})^\top$. We obtain:

$$n_c(\mathbf{x}_k) \approx z_k - \mathbf{H}_k \mathbf{x}_k \tag{50}$$

with quantities z_k and $\mathbf{H}_k$, which are given by:

$$z_k = n_c(\mathbf{x}_{k|k-1}) + \mathbf{H}_k \mathbf{x}_{k|k-1} \tag{51}$$

$$\mathbf{H}_k = -\frac{\partial n_c(\mathbf{x}_k)}{\partial \mathbf{x}_k}\bigg|_{\mathbf{x}_k = \mathbf{x}_{k|k-1}} \tag{52}$$

$$= \left(\frac{-v_p h_p^2 \cos\varphi_{k|k-1}}{r_{k|k-1}^2 \sqrt{r_{k|k-1}^2 - h_p^2}}, \; \frac{v_p \sin\varphi_{k|k-1} \sqrt{r_{k|k-1}^2 - h_p^2}}{r_{k|k-1}}, \; -1, \; 0 \right). \tag{53}$$

The notation chosen indicates that the effect of the GMTI-specific clutter notch on the likelihood function can formally be described by a fictitious measurement z_k and a corresponding fictitious measurement matrix $\mathbf{H}_k$. The real measurements are denoted by $\mathbf{z}_k^i$. By these considerations the detection probability $P_D(\mathbf{x}_k)$ can thus approximated by using a GAUSSian, which *linearly* depends on the target's kinematical state vector $\mathbf{x}_k$:

$$P_D(\mathbf{x}_k) \approx p_D(r_{k|k-1}, \varphi_{k|k-1}) \left[1 - \frac{\mathrm{MDV}}{\sqrt{\log 2/\pi}} \, \mathcal{N}\left(z_k; \, \mathbf{H}_k \mathbf{x}_k, \, \frac{\mathrm{MDV}^2}{2 \log 2}\right) \right]. \tag{54}$$

with a fictitious standard deviation of the measurement error related to z_k essentially given by the minimum detectable velocity (MDV), being a characteristic sensor parameter of the STAP radar.

In order to simplify the notation we introduce quantities $\mathbf{z}_k^{nj}$, $\mathbf{H}_k^{nj}$, $\mathbf{R}^{nj}$ defined by:

$$\begin{array}{lll} \mathbf{z}_k^{01} = z_k, & \mathbf{H}_k^{01} = \mathbf{H}_k, & \mathbf{R}^{01} = \frac{\mathrm{MDV}^2}{2\log 2} \\ \mathbf{z}_k^{n0} = \mathbf{z}_k^n, & \mathbf{H}_k^{n0} = \mathbf{H}, & \mathbf{R}^{n0} = \mathbf{R}, \qquad n = 1, \ldots, n_k \\ \mathbf{z}_k^{n1} = (\mathbf{z}_k^n, z_k)^\top, & \mathbf{H}_k^{n1} = (\mathbf{H}, \mathbf{H}_k)^\top, & \mathbf{R}^{n1} = \mathrm{diag}\left[\mathbf{R}, \frac{\mathrm{MDV}^2}{2\log 2}\right], \quad n = 1, \ldots, n_k. \end{array} \tag{55}$$

We formally introduce $\mathbf{R}^{00} = \infty$. According to the previous approximation the likelihood function $p(Z_k, n_k|\mathbf{x}_k)$ can therefore be written as a weighted sum of GAUSSians:

$$p(Z_k, n_k|\mathbf{x}_k) \propto \sum_{n=0}^{n_k} \sum_{j=0}^{1} \pi_k^{nj}\, \mathcal{N}\left(\mathbf{z}_k^{nj};\, \mathbf{H}_k^{nj}\mathbf{x}_k,\, \mathbf{R}^{nj}\right) \tag{56}$$

with weighting factors given by ($n = 1, \ldots, n_k$):

$$\pi_k^{00} = \rho_F[1 - p_D(r_{k|k-1}, \varphi_{k|k-1})], \qquad \pi_k^{01} = p_D(r_{k|k-1}, \varphi_{k|k-1})\, \rho_F\, \frac{\mathrm{MDV}}{\sqrt{\log 2/\pi}} \tag{57}$$

$$\pi_k^{n0} = p_D(r_{k|k-1}, \varphi_{k|k-1}), \qquad \pi_k^{n1} = -p_D(r_{k|k-1}, \varphi_{k|k-1})\, \frac{\mathrm{MDV}}{\sqrt{\log 2/\pi}} \tag{58}$$

2.4.2 Filtering Process

According to BAYES' rule the processing of the new sensor data Z_k received at revisit time t_k is based on the predicted density $p(\mathbf{x}_k|\mathcal{Z}^{k-1})$ and the likelihood function $p(Z_k, n_k|\mathbf{x}_k)$. With equation 56 we obtain up to a normalizing constant:

$$p(\mathbf{x}_k|\mathcal{Z}^k) \propto p(Z_k, n_k|\mathbf{x}_k)\; p(\mathbf{x}_k|\mathcal{Z}^{k-1}) \tag{59}$$

$$\propto \sum_{n=0}^{n_k} \sum_{i,j=0}^{1} p_{k-1}^i\, \pi_k^{nj}\, \mathcal{N}\left(\mathbf{z}_k^{nj};\, \mathbf{H}_k^{nj}\mathbf{x}_k,\, \mathbf{R}^{nj}\right) \mathcal{N}\left(\mathbf{x}_k;\, \mathbf{x}_{k|k-1}^i,\, \mathbf{P}_{k|k-1}^i\right). \tag{60}$$

The product of GAUSSians in Equation 60 can be rewritten according to the following product formula:

$$\mathcal{N}\left(\mathbf{z};\, \mathbf{H}\mathbf{x},\, \mathbf{R}\right)\; \mathcal{N}\left(\mathbf{x};\, \mathbf{y},\, \mathbf{P}\right) = \mathcal{N}\left(\mathbf{x};\, \mathbf{H}\mathbf{y},\, \mathbf{S}\right)\; \mathcal{N}\left(\mathbf{x};\, \mathbf{y} + \mathbf{W}(\mathbf{z} - \mathbf{H}\mathbf{y}),\, \mathbf{P} - \mathbf{W}\mathbf{S}\mathbf{W}\right) \tag{61}$$

$$\text{where} \qquad \mathbf{S} = \mathbf{H}\mathbf{P}\mathbf{H}^\top + \mathbf{R}, \qquad \mathbf{W} = \mathbf{P}\mathbf{H}^\top\mathbf{S}^{-1} \tag{62}$$

with compatible vectors and matrices $\mathbf{x}$, $\mathbf{y}$, $\mathbf{z}$, $\mathbf{H}$, $\mathbf{P}$, $\mathbf{R}$. This formula is a consequence of the observation that the left hand side of Equation 61 can be interpreted as a joint density $p(\mathbf{z}, \mathbf{x}) = p(\mathbf{z}|\mathbf{x})p(\mathbf{x})$. The right hand side is follows by computing $p(\mathbf{x}|\mathbf{z})$ and $p(\mathbf{z})$. We thus obtain $p(\mathbf{x}_k|\mathcal{Z}^k)$ as a GAUSSian mixture

$$p(\mathbf{x}_k|\mathcal{Z}^k) \propto \sum_{n=0}^{n_k} \sum_{i,j=0}^{1} p_k^{nij}\, \mathcal{N}\left(\mathbf{x}_k;\, \mathbf{x}_{k|k}^{nij},\, \mathbf{P}_{k|k}^{nij}\right) \tag{63}$$

with mixture parameters p_n^{nij}, $\mathbf{x}_{k|k}^{nij}$, and $\mathbf{P}_{k|k}^{nij}$ given by the KALMAN-type following update equations:

$$p_k^{nij} = q_k^{nij} \,/ \textstyle\sum_{n=0}^{n_k} \sum_{i,j=0}^{1} q_k^{nij} \tag{64}$$

$$q_k^{0i0} = p_{k-1}^i \pi^{00}, \qquad q_k^{nij} = p_{k-1}^i \pi_k^{nj}\, \mathcal{N}\left(z_k^{nj};\, \mathbf{H}_k^{nj}\mathbf{x}_{k|k-1}^i,\, \mathbf{S}_{k|k-1}^{nij}\right) \tag{65}$$

$$\mathbf{x}_{k|k}^{0i0} = \mathbf{x}_{k|k-1}^i \qquad \mathbf{x}_{k|k}^{nij} = \mathbf{x}_{k|k-1}^i + \mathbf{W}_{k|k-1}^{nij}\left(\mathbf{z}_k^{nj} - \mathbf{H}_k^{nj}\mathbf{x}_{k|k-1}^i\right) \tag{66}$$

$$\mathbf{P}_{k|k}^{0i0} = \mathbf{P}_{k|k-1}^i \qquad \mathbf{P}_{k|k}^{nij} = \mathbf{P}_{k|k-1}^i - \mathbf{W}_{k|k-1}^{nij}\mathbf{S}_k^{nij}\mathbf{W}_{k|k-1}^{nij\top} \tag{67}$$

$$\mathbf{W}_{k|k-1}^{nij} = \mathbf{P}_{k|k-1}^i\mathbf{H}_k^{nj\top}\mathbf{S}_k^{nij^{-1}} \qquad \mathbf{S}_k^{nij} = \mathbf{H}_k^{nj}\mathbf{P}_{k|k-1}^i\mathbf{H}_k^{nj\top} + \mathbf{R}_{k|k-1}^{nj}. \tag{68}$$

2.4.3 Realization Aspects

The probability density $p(\mathbf{x}_k|\mathcal{Z}^k)$ (equation 63) is a mixture with $4(n_k + 1)$ components. If it is propagated according to the BAYESian formalism, an exponential growth of the number of mixture components seems to be inevitable.

Following the spirit of the techniques used in standard PDA or IMM methods previously discussed, we propose a suboptimal approach for keeping the number of mixture components under control, which might easily be refined if required. Let us first consider the following second-order approximation:

$$p(\mathbf{x}_k|\mathcal{Z}^k) \approx \sum_{i=0}^{1} p_k^i \; p_i(\mathbf{x}_k) \quad \text{with} \quad p_i(\mathbf{x}_k) = \frac{1}{p_k^i} \sum_{n=0}^{n_k} p_k^{ni} \; \mathcal{N}\left(\mathbf{x}_k; \, \mathbf{x}_k^{ni}, \, \mathbf{P}_k^{ni}\right) \tag{69}$$

where the quantities p_k^{ni}, p_k^i, $\mathbf{x}_k^{ni}$, and $\mathbf{P}_k^{ni}$ are given by moment matching.

The mixture components that define the individual densities $p_i(\mathbf{x}_k)$ are related to the data interpretations due to the uncertainty regarding the origin of the reports. They may be handled by well-established mixture reduction techniques discussed in the previous talk (subsection 3.5). Provided the clutter density is low, a second-order approximation of each $p_i(\mathbf{x}_k)$ seems to be reasonable and results in a GAUSSian (standard PDA). For the sake of simplicity this approach has been used in the numerical results presented below. Hence the $p(\mathbf{x}_k|\mathcal{Z}^k)$ is finally approximated by a normal mixture with two components at each time t_k. The generalization to more refined approximation techniques is straightforward and leads to MHT (Multiple Hypothesis Tracking).

2.5 Discussion

Figures 11 – 16 provide a qualitative insight into the effect of the refined sensor model on target tracking/data fusion. While a high adaptivity is evident near the clutter notch, far from the notch no difference to standard filters is observed.

2.5.1 Effect of GMTI-Modeling

Figures 11a, 11b display the probability density functions resulting from processing the event that a missing detection occurred near the notch. To show the most interesting features, the densities are projected on the azimuth/ range-rate plane. While the pdf of the standard tracker (Figure 11a) is identical with the corresponding predicted density, the refined sensor model leads to a bimodal structure (Figure 11b). The broader peak refers to the possible event that the missing detection has simply statistical reasons as in case of standard filtering, while the sharper peak behind it reflects the hypothesis that the target was not detected because it is masked by the clutter notch. The situation that the target is buried in the clutter notch for several revisits is represented in Figures 12a, 12b. Evidently the pdf of the standard filter totally faded away permitting no reasonable state estimation (Figure 12a). The refined filter, however, preserved a definite shape (Figure 12b). This can be explained as follows: Instead of actual sensor data the very information that several successively missing detections occurred was processed. This event provides a hint to the filter that the kinematical target state probably obeys a certain relation determined by the clutter notch. Apparently, this piece of evidence proves to be as valuable as a measurement of one of the components of the target state. Figures 13a, 13b refer to the event that a detection occurred near the clutter notch. While the standard filter produced a simple GAUSSian, the refined filter shows a more complex structure. In fact, the pdf is a two-component mixture whose weighting factors differ in their sign (but sum up to one). The resulting shape permits an intuitive interpretation: The sensor model inherently takes into account that the target state $\mathbf{x}_k$ does not lead to a small value of $n_c(\mathbf{x}_k)$; otherwise the target would not have been detected at all. For this reason, the sharp cut in the pdf simply indicates the location of the clutter notch.

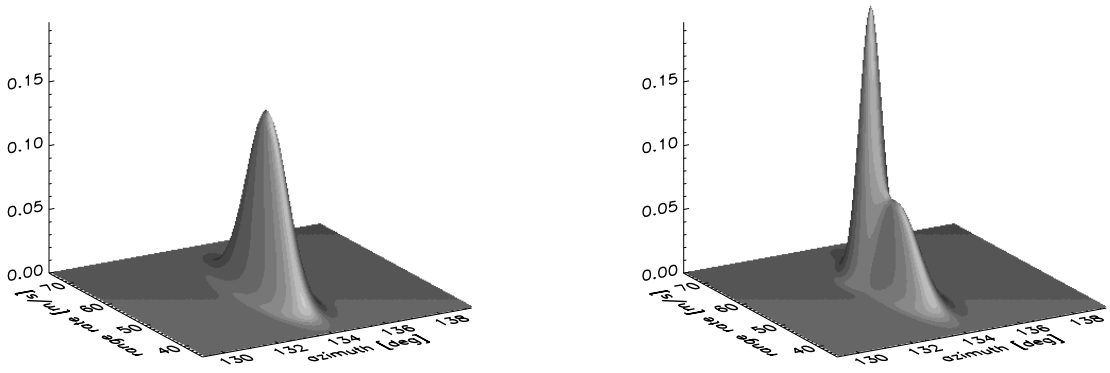

Figure 11: (a) standard filter (b) GMTI filter (no detection)

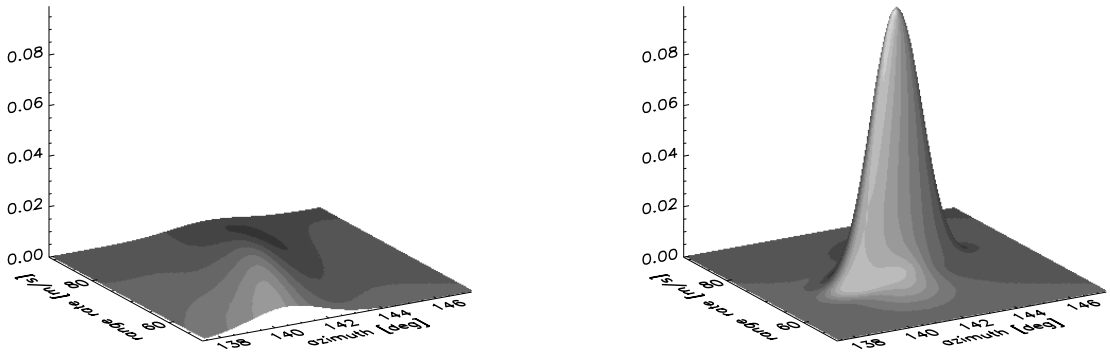

Figure 12: (a) standard filter (b) GMTI filter (within the notch)

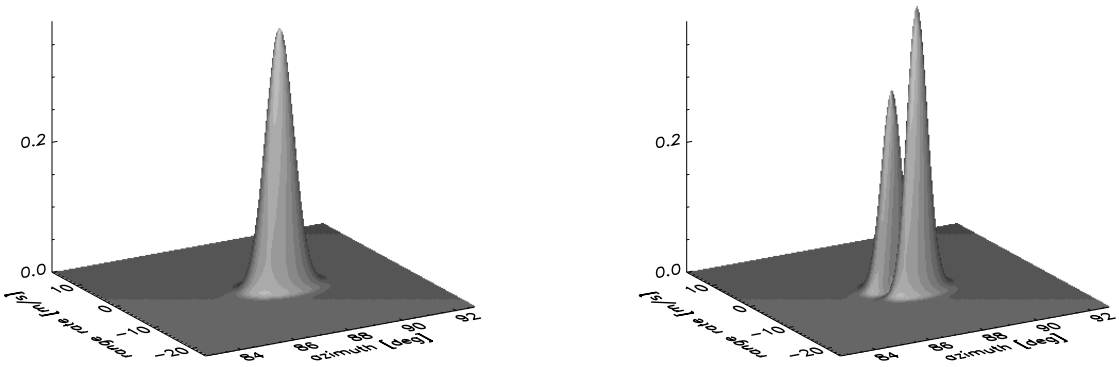

Figure 13: (a) standard filter (b) GMTI filter (detection near the notch)

2.5.2 Gain by Sensor Data Fusion

Figures 14 – 16 show the probability densities of the target position in Cartesian ground coordinates after filtering. The prolated structure of the pdfs mirrors the predominant impact of cross-range errors. Their shape is rotated with respect to each other due to the different sensor/target geometries. This effect can be much more pronounced in other situations. We indicated the true target position. Figures 14a – 16a refer to a regular tracking situation (after 10 min, see Figures 7, 8). Doppler-blindness occurred for sensor 2 during the previous revisits. The probability densities shown in Figure 14b – 16b have been calculated at a time when the target has stopped for 3 min (Figure 8). Evidently in Figures 14b, 15b the dissipation of the density functions is confined to a particular direction according to the GMTI sensor model. Figures 16a, 16b show the probability densities obtained by sensor data fusion. In both cases we observe a significant fusion gain. It is a consequence of the different orientation of the density functions and leads to improved state estimates. The result for the stopping targets is particularly remarkable. Though no sensor data are available from both sensors, the very fusion of the sensor output 'target under track is no longer detected' implies an improved target localization. This is a consequence of the different target/sensor geometries.

3 Fusion with Context Information: Road Maps

In many practical cases even military ground vehicles move on roads, whose topographical coordinates are available up to a certain error (digitized road map information). In this context it seems reasonable to describe the kinematical state vector $\mathbf{x}_k^r$ of road targets at time t_k by its position on the road l_k (i.e. the arc length of the curve) and its scalar speed $\dot{l}_k$: $\mathbf{x}_k^r = (l_k, \dot{l}_k)^\top$. The model for describing the dynamical behavior of road targets is therefore a 2D version of equation 41. By making use of the related transition density $p(\mathbf{x}_k^r|\mathbf{x}_{k-1}^r)$ the predicted density in road coordinates is given by $p(\mathbf{x}_k^r|\mathcal{Z}^{k-1}) = \int d\mathbf{x}_{k-1}^r \; p(\mathbf{x}_k^r|\mathbf{x}_{k-1}^r) \; p(\mathbf{x}_{k-1}^r|\mathcal{Z}^{k-1})$.

3.1 Modelling of Roads

A given road through a real road network is mathematically described by a continuous 3D curve $\mathcal{R}^*$ in Cartesian ground coordinates. For the sake of simplicity the effect of crossroads is not considered here. See [21, 22] for a more detailed discussion. Let $\mathcal{R}^*$ be parameterized by the corresponding arc length l. The exploitation of digitized road maps provides the data base for a piecewise linear approximation of the road curve $\mathcal{R}^* : l \mapsto \mathcal{R}^*(l)$ by a polygonal curve $\mathcal{R}$. Let us furthermore assume that the curve $\mathcal{R}$ is characterized by n_r node vectors

$$\mathbf{s}_m = \mathcal{R}^*(l_m), \quad m = 1, \ldots, n_r. \tag{70}$$

From the these quantities $n_r - 1$ normalized tangential vectors

$$\mathbf{t}_m = (\mathbf{s}_{m+1} - \mathbf{s}_m)/||\mathbf{s}_{m+1} - \mathbf{s}_m||, \quad m = 1, \ldots, n_r - 1 \tag{71}$$

can be derived. The EUCLIDian distance $||\mathbf{s}_{m+1} - \mathbf{s}_m||$ between two adjacent node vectors, however, is usually not identical with the distance $\lambda_m = l_{m+1} - l_m$ actually covered by a vehicle when it moves from $\mathbf{s}_m$ to $\mathbf{s}_{m+1}$ along the road. Besides the vectors $\mathbf{s}_m$ the scalar quantities $\lambda_m \geq |\mathbf{s}_{m+1} - \mathbf{s}_m|$ should therefore enter into the road model to make it more realistic. The differences $\sigma_d = |\lambda_m - ||\mathbf{s}_{m+1} - \mathbf{s}_m||\,|$ can evidently serve as a quantitative measure of the discretization errors we have to deal with. Using the characteristic functions

$$\chi_m(l) = \begin{cases} 1 & \text{for } l \in (l_m, l_{m+1}) \\ 0 & \text{else} \end{cases}, \quad m = 0, \ldots, n_r, \quad l_0 = -\infty, \quad l_{n_r+1} = \infty \tag{72}$$

$$\text{and} \quad \mathbf{s}_0 = \mathbf{s}_1, \quad \mathbf{t}_0 = \mathbf{t}_1, \quad l_0 = l_1, \quad \mathbf{t}_{n_r} = \mathbf{t}_{n_r-1}, \tag{73}$$

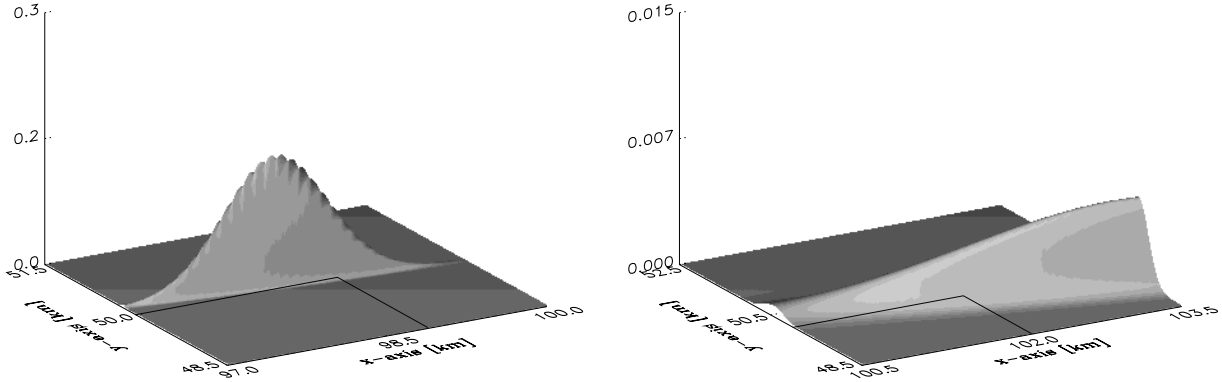

Figure 14: (a) tracking (b) target stop (sensor 1)

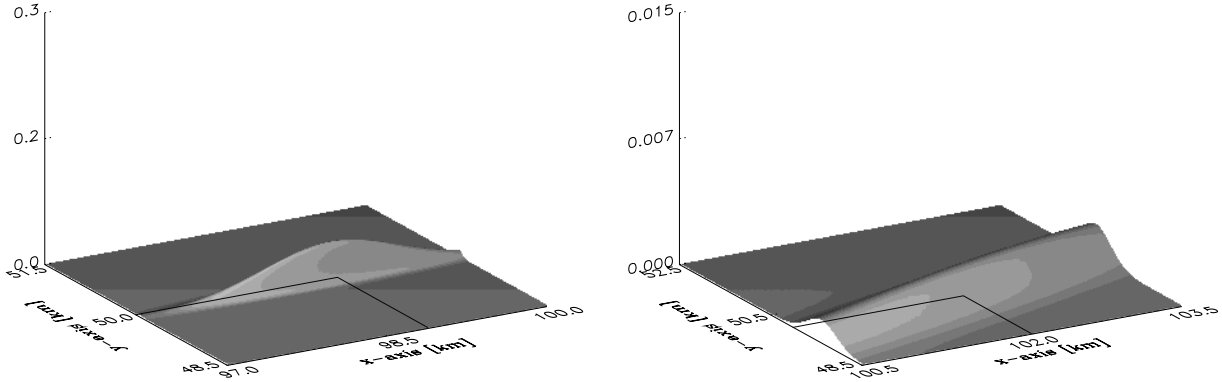

Figure 15: (a) tracking (b) target stop (sensor 2)

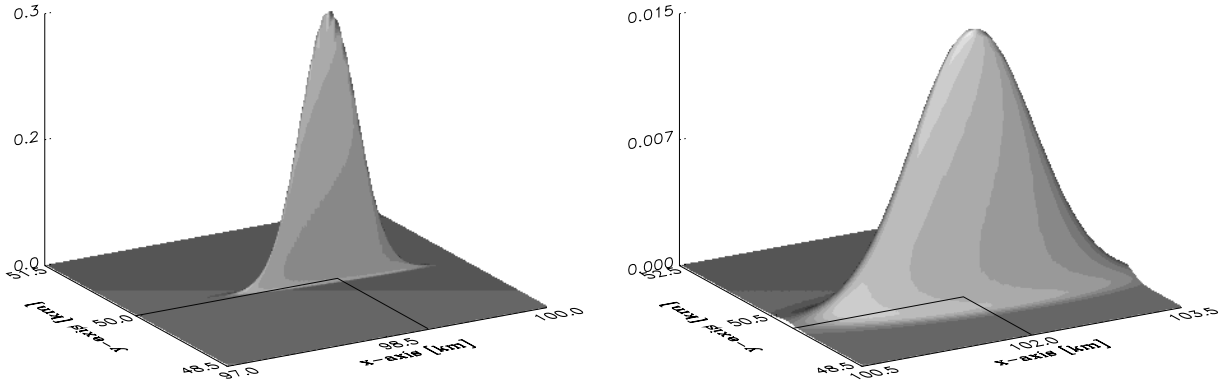

Figure 16: (a) tracking (b) target stop (sensor 1+2)

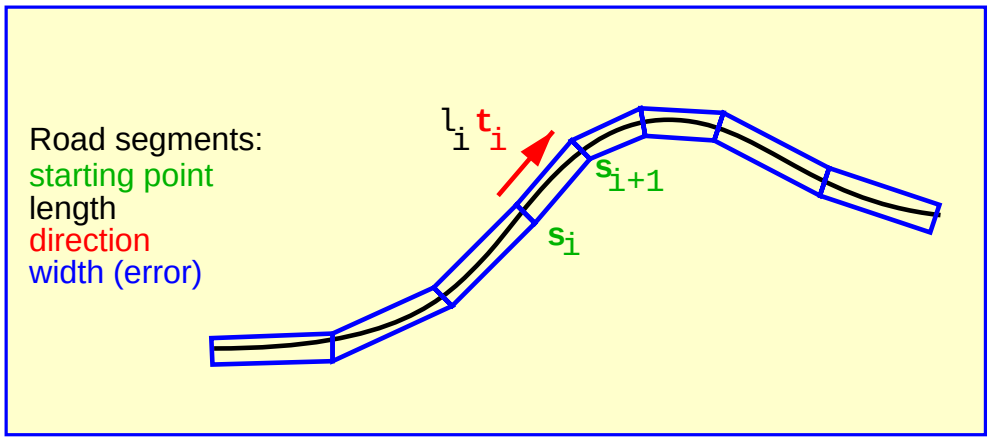

Figure 17: Schematic Representation of a Road

we obtain a mathematically simple description of the polygon curve $\mathcal{R}$, by which the road $\mathcal{R}^*$ is approximated:

$$\mathcal{R} : l \mapsto \mathcal{R}(l) = \sum_{m=0}^{n_r} \left[\mathbf{s}_m + (l - l_m)\mathbf{t}_m\right] \chi_m(l) \tag{74}$$

$$\text{with:} \quad \mathcal{R}^*(l_m) = \mathcal{R}(l_m) = \mathbf{s}_m, \quad m = 0, \ldots, n_r. \tag{75}$$

3.2 Densities on Roads

The BAYESian formalism previously discussed can directly be applied to road targets, if it is possible to find a transformation operator $\mathcal{T}_{g\leftarrow r}$ by which the predicted density $p(\mathbf{x}_k^r|\mathcal{Z}^{k-1})$ in road coordinates can be transformed into ground coordinates:

$$p(\mathbf{x}_k^g|\mathcal{Z}^{k-1}) = \mathcal{T}_{g\leftarrow r}[p(\mathbf{x}_k^r|\mathcal{Z}^{k-1})]. \tag{76}$$

When available in ground coordinates, the linearized versions of the transforms $\mathbf{t}_{s\leftarrow g}$ and $\mathbf{t}_{g\leftarrow s}$ (section 2.1) can be used to represent the densities in sensor coordinates, where the filtering step is performed. To this end, we write the density $p(\mathbf{x}_k^g|\mathcal{Z}^{k-1})$ as a sum over the $n_r + 1$ road segments considered:

$$p(\mathbf{x}_k^g|\mathcal{Z}^{k-1}) = \sum_{m=0}^{n_r} p(\mathbf{x}_k^g, m|\mathcal{Z}^{k-1}) \tag{77}$$

$$= \sum_{m=0}^{n_r} p(\mathbf{x}_k^g|m, \mathcal{Z}^{k-1})\, p(m|\mathcal{Z}^{k-1}) \tag{78}$$

$$= \sum_{m=0}^{n_r} p_{g\leftarrow r}^m\, \mathcal{T}_{g\leftarrow r}^m\left[p(\mathbf{x}_k^r|\mathcal{Z}^{k-1})\right]. \tag{79}$$

In equation 79 the probability

$$p(m|\mathcal{Z}^{k-1}) = \int d\mathbf{x}_k^r\, p(m, \mathbf{x}_k^r|\mathcal{Z}^{k-1}) \tag{80}$$

$$= \int d\mathbf{x}_k^r\, \chi_m(\mathbf{H}_r\mathbf{x}_k^r)\, p(\mathbf{x}_k^r|\mathcal{Z}^{k-1}) \tag{81}$$

$$=: p_{g\leftarrow r}^m \tag{82}$$

denotes the probability that the target moves on the segment m given the accumulated sensor data $\mathcal{Z}^{k-1}$. The matrix $\mathbf{H}_r$ is defined by $\mathbf{H}_r \mathbf{x}_k^r = l_k$. Later on, it will be intuitively interpreted as a fictitious measurement matrix. Since the density $p(\mathbf{x}_k^r|\mathcal{Z}^{k-1}) = \sum_{j=0}^{1} p_{k-1}^j \; \mathcal{N}\left(\mathbf{x}_k^r; \mathbf{x}_{k|k-1}^{rj}, \mathbf{P}_{k|k-1}^{rj}\right)$ is a GAUSSian mixture due to the GMTI sensor model, the probabilities $p_{g\leftarrow r}^m$ can explicitly be expressed by error functions:

$$p_{g\leftarrow r}^m = p_{k-1}^j \left(\Phi[\lambda(l_{m+1}^j)] - \Phi[\lambda(l_m^j)]\right), \quad m = 0, \ldots, n_r \tag{83}$$

with:

$$\Phi(\lambda) = 1/\sqrt{2\pi} \int_{-\infty}^{\lambda} dt \; \exp(-t^2/2) \tag{84}$$

$$\lambda(l)^j = \frac{l - \mathbf{H}_r \mathbf{x}_{k|k-1}^{rj}}{\sqrt{\mathbf{H}_r \mathbf{P}_{k|k-1}^{rj} \mathbf{H}_r^\top}}. \tag{85}$$

For the remaining term in equation 79 standard probability reasoning yields:

$$\begin{aligned} \mathcal{T}_{g\leftarrow r}^m \left[p(\mathbf{x}_k^r|\mathcal{Z}^{k-1})\right] &= p(\mathbf{x}_k^g|m, \mathcal{Z}^{k-1}) && (86)\\ &= \int d\mathbf{x}_k^r \; p(\mathbf{x}_k^g, \mathbf{x}_k^r|m, \mathcal{Z}^{k-1}) && (87)\\ &= \int d\mathbf{x}_k^r \; p(\mathbf{x}_k^g|\mathbf{x}_k^r, m) \; p(\mathbf{x}_k^r|m, \mathcal{Z}^{k-1}). && (88) \end{aligned}$$

3.2.1 Simple Roads

Let us first consider the simple limiting case of a straight road defined by: $\mathcal{R}(l) = \mathbf{s} + l\mathbf{t}$. Under GAUSSian assumptions the transform from road to ground coordinates is defined by the normal transition density: $p(\mathbf{x}_{k+1}^g|\mathbf{x}_{k+1}^r) = \mathcal{N}\left(\mathbf{x}_{k+1}^g; \mathbf{t}_{g\leftarrow r}[\mathbf{x}_{k+1}^r], \sigma_m^2\right)$ with the affine transform $\mathbf{t}_{g\leftarrow r}[\mathbf{x}_r] = \left(\begin{smallmatrix} \mathbf{t} & 0 \\ 0 & \mathbf{t} \end{smallmatrix}\right)\mathbf{x}_r + \left(\begin{smallmatrix} \mathbf{s}-l\mathbf{t} \\ 0 \end{smallmatrix}\right)$ and σ_m denoting the standard deviation of the mapping error. The transformation of the density $p(\mathbf{x}_k^r|\mathcal{Z}^{k-1})$ into the ground coordinate system is therefore described by $p(\mathbf{x}_k^g|\mathcal{Z}^{k-1}) = \int d\mathbf{x}_k^r \; p(\mathbf{x}_k^g|\mathbf{x}_k^r) \; p(\mathbf{x}_k^r|\mathcal{Z}^{k-1})$. The integration can explicitly be carried out and preserves the GAUSSian character of the density functions (normal mixtures). The corresponding inverse is simply provided by a projection of the density $p(\mathbf{x}_k^g|\mathcal{Z}^{k-1})$ on the road. With these transformations the previous considerations directly apply.

3.2.2 Polygonal Roads

The transition density $p(\mathbf{x}_k^g|\mathbf{x}_k^r, m)$ for the road segment m (equation 88) is characterized by road map and discretization errors (σ_m, σ_d), that may vary from segment to segment. Under GAUSSian assumptions regarding the possible error sources, with the affine transforms $\mathbf{t}_{g\leftarrow r}^m[\mathbf{x}_r] = \left(\begin{smallmatrix} \mathbf{t}_m & 0 \\ 0 & \mathbf{t}_m \end{smallmatrix}\right)\mathbf{x}_r + \left(\begin{smallmatrix} \mathbf{s}_m - l_m\mathbf{t}_m \\ 0 \end{smallmatrix}\right)$ for each individual road segment m, and the error standard deviation $\sigma_r^2 = \sigma_m^2 + \sigma_d^2$, we obtain normal transition densities

$$p(\mathbf{x}_g|\mathbf{x}_r, m) = \mathcal{N}\left(\mathbf{x}_g; \mathbf{t}_{g\leftarrow r}^m[\mathbf{x}_r], \sigma_r^2\right). \tag{89}$$

With these preliminaries, an application of BAYES' rule to the remaining density in the integrand of equation 88 yields:

$$p(\mathbf{x}_k^r|m, \mathcal{Z}^{k-1}) = \frac{p(m|\mathbf{x}_k^r) \; p(\mathbf{x}_k^r|\mathcal{Z}^{k-1})}{\int d\mathbf{x}_k^r \; p(m|\mathbf{x}_k^r) \; p(\mathbf{x}_k^r|\mathcal{Z}^{k-1})} \tag{90}$$

with probabilities $p(m|\mathbf{x}_k^r)$ given by:

$$p(m|\mathbf{x}_k^r) = \chi_m(\mathbf{H}_r \mathbf{x}_k^r). \tag{91}$$

Up to now the derivation was exact. Due to the normalization constant, however, the characteristic functions violate the GAUSSian character of the probability densities. To circumvent this problem we propose the following normal approximation:

$$p(m|\mathbf{x}_k^r) \approx \exp[-\tfrac{1}{2}(z_r^m - \mathbf{H}_r\mathbf{x}_r)^2/\lambda_m^2] = \sqrt{2\pi}\lambda_m \; \mathcal{N}\left(z_r^m;\, \mathbf{H}_r\mathbf{x}_r,\, \lambda_m^2\right) \tag{92}$$

with z_r^m and λ_m^2 given by:

$$z_r^m = \tfrac{1}{2}(l_{m+1} + l_m) \tag{93}$$

$$\lambda_m^2 = \frac{(l_{m+1} - l_m)^2}{12}. \tag{94}$$

The quantities z_r^m and λ_m^2 can be interpreted as the mean and variance of a uniform density given by $\chi_m(l)$. From equation 91 and the product formula (section 4.3) we obtain:

$$p(\mathbf{x}_k^r|m, \mathcal{Z}^{k-1}) = \sum_{j=0}^{1} p_{k-1}^m \; \mathcal{N}\left(\mathbf{x}_k^r;\, \mathbf{x}_{k|k-1}^{rmj},\, \mathbf{P}_{k|k-1}^{rmj}\right) \tag{95}$$

with KALMAN-type update equations for $\mathbf{x}_{k|k-1}^{rmj}$ and $\mathbf{P}_{k|k-1}^{rmj}$, where z_r^m, λ_m^2 are in analogy to a measurement and a related measurement error variance:

$$\mathbf{x}_{k|k-1}^{rmj} = \mathbf{x}_{k|k-1}^{rj} + \mathbf{W}_r^{mj}(z_r^m - \mathbf{H}_r\mathbf{x}_{k|k-1}^{rmj}) \tag{96}$$

$$\mathbf{P}_{k|k-1}^{rmj} = \mathbf{P}_{k|k-1}^{rmj} - \mathbf{W}_r^{mj}\mathbf{S}_r^{mj}\mathbf{W}_r^{mj\top}. \tag{97}$$

with "innovation" covariance matrices $\mathbf{S}_r^{mj}$ and "KALMANGain" matrices $\mathbf{W}_r^{mj}$ given by:

$$\mathbf{S}_r^{mj} = \mathbf{H}_r\mathbf{P}_{k|k-1}^{rmj}\mathbf{H}_r^\top + \lambda_m^2 \tag{98}$$

$$\mathbf{W}_r^{mj} = \mathbf{P}_{k|k-1}^{rmj}\mathbf{H}_r^\top\mathbf{S}_r^{mj^{-1}} \tag{99}$$

The notation chosen indicates that the effect of road map information on the probability density functions can formally be described by a fictitious measurement, a corresponding measurement matrix, and a fictitious measurement error. Now the integration in equation88 can be carried out explicitly as in the previously discussed limiting case. The transformation from road to ground coordinates is thus known. In analogy to the limiting case of straight roads, the inverse transform is simply provided by individually projecting the densities $p(\mathbf{x}_k^g|m, \mathcal{Z}^k)$ on the road (i.e. after the filtering step has been performed). Before the subsequent prediction is performed, it seem to be reasonable to apply a second-order approximation to the mixture densities:

$$p(\mathbf{x}_k^r|\mathcal{Z}^k) = \sum_{m=0}^{n_r} p(m|\mathcal{Z}^k)\; p(\mathbf{x}_k^r|m, \mathcal{Z}^k) \tag{100}$$

$$\approx \sum_{i=0}^{1} p_k^i \; \mathcal{N}\left(\mathbf{x}_k^r;\, \mathbf{x}_{k|k}^{ri},\, \mathbf{P}_{k|k}^{ri}\right). \tag{101}$$

References

[1] ABRAMOWITZ, M., SEGUN, I.A., *Handbook of Mathematical Functions*, Dover (1965).

[2] BAR-SHALOM, Y., LI, X.-R., AND KIRUBARAJAN, T., *Estimation with Applications to Tracking and Navigation*, Wiley & Sons, 2001.

[3] BOGLER, P.L., *Radar Principles with Applications to Tracking Systems*, John Wiley & Sons (1990).

[4] DEMPSTER, R.J., BLACKMAN, S.S., ROSZKOWSKI, S.H., SASAKI, D.M., 'IMM/MHT Solution to Radar and Multisensor Benchmark Tracking Problems', *SPIE **3373**, Signal and Data Processing of Small Targets* (1998).

[5] BLAIR, W.D., WATSON,G.A., KIRUBARAJAN,T., BAR-SHALOM, Y., 'Benchmark for Radar Resource Allocation and Tracking Targets in the Presence of ECM', *IEEE AES **35***, No. 4 (1998).

[6] BLAIR, W.D., WATSON, G.A., KOLB, K.W., 'Benchmark Problem for Beam Pointing Control of Phased-Array Radar in the Presence of False Alarms and ECM', *Proceedings 1995 American Control Conference*, Seattle WA (1994).

[7] VAN KEUK, 'Multihypothesis Tracking with Electronically Scanned Radar', *IEEE AES **31***, No. 3 (1995).

[8] VAN KEUK, G., BLACKMAN, S., 'On Phased-Array Tracking and Parameter Control', *IEEE AES **29***, No. 1 (1993).

[9] KIRUBARAJAN, T., BAR-SHALOM, Y., PATTIPATI, K.R., KADAR, I., 'Ground Target Tracking with Variable Structure IMM Estimator', *IEEE Transactions on Aerospace and Electronic Systems*, **AES-36**, 26 (2000).

[10] KIRUBARAJAN, T., BAR-SHALOM, Y., PATTIPATI, K.R., KADAR, I., 'Large Scale Ground Target Tracking With Single and Multiple MTI Sensors', Chapter 6 in: Y. Bar-Shalom, Blair, W.D. (Eds.), *Multitarget-Multisensor Tracking Applications and Advances III*, Boston, MA: Artech House, 2000.

[11] KIRUBARAJAN, T., BAR-SHALOM, Y., BLAIR, W.D., WATSON, G.A., 'IMMPDAF Solution to Benchmark for Radar Resource Allocation and Tracking Targets in the Presence of ECM', *IEEE AES **35***, No. 4 (1998).

[12] KLEMM, R., 'Ground moving target tracking with STAP radar: the sensor' MTI Sensors', Chapter V.1 in: R. Klemm (Ed.), *Applications of Space-Time Adaptive Processing*, *IEE Publishers*, London, UK, 2003.

[13] KLEMM, R., 'Principles of space-time adaptive processing', London, UK, *IEE Publishers*, 2002.

[14] KOCH, W., Ground Target Tracking with STAP Radar: Selected Tracking Aspects. Chapter 15 in: R. KLEMM (Ed.), *The Applications of Space-Time Adaptive Processing*, IEE Publishers, 2004.

[15] KOCH, W., 'Expectation Maximization for GMTI Convoy Tracking', Proceedings of: *SPIE Signal and Data Processing of Small Targets 2002*, Vol. 4728, pp. 450-460, April 2002.

[16] KOCH, W., 'Fixed-Interval Retrodiction Approach to Bayesian IMM-MHT for Maneuvering Multiple Targets', *IEEE Transactions on Aerospace and Electronic Systems*, **36**, No. 1, (2000).

[17] KOCH, W., 'On Adaptive Parameter Control for Phased-Array Tracking', *Signal and Data Processing of Small Targets*, **SPIE Vol. 3809**, pp. 444-455, Denver, USA, July 1999.

[18] KOCH, W., KLEMM, R., 'Ground Target Tracking with STAP Radar', *IEE Proceedings Radar, Sonar and Navigation Systems*, Special Issue: Modeling and Simulation of Radar Systems, 2001, Vol. 148, No. 3, invited paper.

[19] KOCH, W., KEUK, G. VAN, 'On Bayesian IMM-Tracking for Phased-Array Radar', Proceedings of the *International Radar Symposium IRS'98*, pp. 715-723, Mnchen, Germany, September 1998.

[20] SARUNIC, P.W., EVANS, R.J., 'Adaptive Update Rate Tracking using IMM Nearest Neighbour Algorithm Incorporating Rapid Re-Looks', *IEE Proc.-Radar, Sonar, Navig.*, **144**, No. 4 (1997).

[21] ULMKE, M., KOCH, W., 'On Road-Map Assisted GMTI Tracking', Proceedings of: *DGON German Radar Symposium GRS'02*, pp. 89-93, Bonn, Germany, September 2002.

[22] ULMKE, M., 'Improved GMTI-Tracking using Road-Maps and Topographical Information', Proceedings of: *SPIE Signal and Data Processing of Small Targets 2003*, Vol. 5204, July 2003.